applied sciences

MDPI

Article

Wear-Induced Nonlinear Dynamic Response of a Face Gear Pair Considering Tooth-Surface Update and Phase-Dependent Backlash

Yufan Yang [1], Yunbo Shen [1,*], Xianlong Peng [2], Peipei Feng [1] and Xuan Liu [3]

[1] School of Mechatronic Engineering, Xi'an Technological University, Xi'an 710021, China; yangyufan@st.xatu.edu.cn (Y.Y.); fpp1112@163.com (P.F.)
[2] College of Mechanical Engineering, Xi'an University of Science and Technology, Xi'an 710054, China
[3] School of Mechanical and Electrical Engineering, Zhoukou Normal University, Zhoukou 466001, China
* Correspondence: syb0315@yeah.net

Abstract

To evaluate the influence of tooth surface wear on face gear dynamics, this study proposes a coupled wear–dynamics modeling method. A phase-dependent backlash model is developed to preserve the meshing-phase modulation induced by nonuniform wear along the meshing path. The wear-updated tooth surface is used to update the time-varying mesh stiffness, loaded transmission error, and backlash. These quantities are then incorporated into a nonlinear dynamic model. For the single-sided working-flank wear considered here, separate drive- and back-side thresholds are defined in an LTE-referenced coordinate. Experimental measurements are used to assess the contact trace and calibrate the effective wear coefficients. The wear-profile comparison uses the calibration dataset and is interpreted as a post-calibration assessment. The dominant low-speed torque-spectrum peak is consistent with the mesh frequency calculated from shaft speed and tooth count; this kinematic check does not independently validate the dynamic model. The nonlinear dynamic responses are evaluated for a prescribed severe-wear state constructed numerically to give a maximum pinion wear depth comparable to the experimental value. The results show that nonuniform wear changes not only the mean backlash level but also the backlash boundary over the meshing phase. Across the 25-point b_0 = 50:2.5:110 μm comparison at W = 1.19 and four tested initial conditions, the phase-dependent model gives displacement RMS values of 47.60–166.50 μm and peak dynamic mesh forces of 7.46–20.42 kN, compared with 39.03–44.11 μm and 3.23–5.74 kN, respectively, for the three scalar models. The 2000-period calculations identify period-3 and period-1 responses at the two representative conditions, with initial-condition dependence at the latter.

Keywords: face gear; tooth wear; phase-dependent backlash; nonlinear dynamics

Check for updates

Received: 24 September 2026
Revised: 30 October 2026
Accepted: 31 October 2026
Published: 4 November 2026

Copyright: © 2026 by the authors. Licensee MDPI, Basel, Switzerland. This article is an open access article distributed under the terms and conditions of the Creative Commons Attribution (CC BY) license.

1. Introduction

A face gear pair, as shown in Figure 1, is a specialized gear transmission composed of a pinion and a face gear. Owing to its compact structure, smooth transmission, and favorable vibration and noise performance, face gear pairs have been applied in helicopter transmission systems and other high-performance drive systems [1–3]. During long-term operation, tooth surface wear is unavoidable and may degrade transmission accuracy, alter meshing characteristics, and increase vibration and noise.

Considerable efforts have been devoted to predicting gear wear and modeling worn tooth surfaces. Based on Archard's wear theory, various approaches, including tooth contact analysis (TCA), loaded tooth contact analysis (LTCA), finite element methods,

and elastohydrodynamic lubrication models, have been used to predict wear depth and worn tooth surface evolution in different gear systems [4–15]. Park et al. developed semi-analytical and approximate methods for predicting hypoid gear wear [4,5]. Peng et al. combined TCA with finite element analysis to calculate face gear wear and investigate its influence on dynamic behavior [11]. Other studies have further considered surface roughness, installation errors, modification parameters, and lubrication conditions in gear wear prediction [6–10,13–15].

In addition to predicting wear depth, the effects of tooth wear on meshing characteristics and dynamic response have attracted increasing attention. Shen et al. investigated the influence of tooth flank wear on time-varying mesh stiffness (TVMS) and further analyzed its effect on the dynamic characteristics of planetary gear systems [16–18]. Mesh stiffness is also a key excitation parameter in gear dynamic analysis, and Chang et al. proposed a robust model for determining the mesh stiffness of cylindrical gears [19]. Liu et al. studied the coupled effects of eccentricity and tooth wear on gear-rotor vibration [20]. In terms of error-induced gear vibration, Liu et al. proposed a method for studying the long-period three-dimensional vibration characteristics of herringbone gears with asymmetric pitch deviation [21]. Zhang et al. developed a friction–wear-coupled prediction model and revealed the influence of wear on nonlinear gear dynamics [22]. Li et al. established coupled wear–dynamics models to investigate the degradation mechanism of gear dynamic performance under worn conditions [23,24]. Recent studies have also considered tooth modification, mesh stiffness and transmission-error variation, lubrication effects, fatigue–wear coupling, temperature effects, backlash degradation, and dynamically updated tooth surfaces in gear wear–dynamics analyses [25–36].

Previous studies have established that wear affects gear dynamics and backlash. Peng et al. investigated the wear-related dynamic response of a face gear pair [11], while Li and Hao studied backlash degradation associated with wear and assembly errors in a harmonic gear drive [36]. However, tooth surface wear is generally nonuniform along the meshing path, especially in face gear drives with complex contact geometry, and may therefore produce backlash that varies with meshing phase. The present study represents this nonuniform face-gear wear as a meshing-phase-dependent backlash input, together with wear-updated time-varying mesh stiffness (TVMS) and loaded transmission error (LTE). The dynamic effect of this representation is assessed against minimum, full-field mean, and phase-average scalar descriptions. The last of these matches the integral mean of the actual periodic interpolation, allowing the effect of clearance-width modulation to be examined at the same mean width. Replacing the phase-dependent variation with a scalar may remove the meshing-phase modulation of the contact boundary and change the predicted displacement response and dynamic mesh force. In addition, when wear is measured only on the working flanks, assigning the clearance increase equally to both sides does not preserve the unworn back-side boundary. The contact law must therefore distinguish the working-side and back-side thresholds in a common LTE-referenced coordinate.

To address this issue, this study establishes a coupled wear–dynamics modeling framework for a worn face gear pair. The worn tooth surface obtained from wear-contact analysis is used to update TVMS, LTE, and wear-induced backlash. In particular, a phase-dependent wear-induced backlash model is developed to preserve the influence of nonuniform wear along the meshing path. The resulting model is incorporated into a nonlinear dynamic model to investigate the dynamic response of the worn face gear pair. The main contributions of this study are as follows:

(1) A coupled wear–dynamics modeling framework is established by linking worn tooth surface evolution to updates of TVMS, LTE, and backlash.

(2) A phase-dependent wear-induced backlash model is proposed to represent the meshing-phase modulation induced by nonuniform tooth surface wear.
(3) The nonlinear response characteristics and the effects of wear-updated TVMS, LTE, and phase-dependent backlash are examined using global response maps, representative dynamic responses, and comparisons with scalar backlash models. An additional torque-based comparison is used to check the dominant mesh-frequency trend.

The remainder of this paper is organized as follows. Section 2 presents the wear-contact analysis, coupled wear–dynamics framework, and nonlinear dynamic model. Section 3 presents the experimental assessment and numerical results. Section 4 discusses the implications and limitations of the results. Finally, Section 5 summarizes the main conclusions.

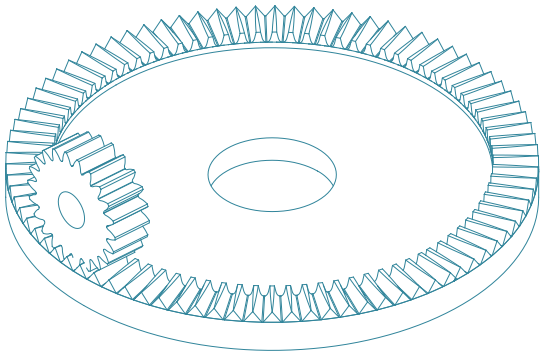


Figure 1. Schematic diagram of the face gear pair.

2. Methods

2.1. Wear-Contact Analysis Model of the Face Gear Pair

This section establishes the wear-contact analysis model of the face gear pair. First, TCA is used to determine the meshing position, contact trace, transmission error, and relative sliding velocity. LTCA is then used to calculate LTE, load distribution, and TVMS. The contact stress is calculated from the contact load and local contact geometry using Hertz contact theory. Finally, the tooth surface wear depth is obtained by combining the contact stress, sliding distance, and Archard wear model.

2.1.1. Tooth Contact Analysis for the Face Gear Pair

According to the meshing principle of the face gear pair, the position and normal vectors of the pinion and face gear tooth surfaces must satisfy the contact conditions at the meshing point. Therefore, the TCA equations can be written as

$$\begin{cases} \boldsymbol{r}_f^{(1)}(u_1, \theta_1, \phi_1') = \boldsymbol{r}_f^{(2)}(u_2, \theta_2, \phi_2'), \\ \boldsymbol{n}_f^{(1)}(u_1, \theta_1, \phi_1') = \boldsymbol{n}_f^{(2)}(u_2, \theta_2, \phi_2'). \end{cases} \tag{1}$$

Here, u_i and θ_i are tooth-surface parameters, ϕ_i' is the rotation parameter used to transform the corresponding surface into the common coordinate system, and $i = 1$ and $i = 2$ denote the pinion and face gear, respectively. The meshing equation can be expressed as

$$f_{s2} = \boldsymbol{n}_s \cdot \boldsymbol{v}_s^{(s2)} = 0. \tag{2}$$

In the generating meshing equation, $\boldsymbol{n}_s$ is the normal to the generating cutter surface and $\boldsymbol{v}_s^{(s2)}$ is the relative velocity between the cutter and face gear, expressed in the cutter coordinate system. TCA provides the contact trace, transmission error, contact ellipse parameters, initial contact clearance, and relative sliding velocity. These quantities are used as geometric and kinematic inputs for the subsequent loaded contact analysis and wear calculation. In

particular, the relative sliding velocity provides the sliding distance in the Archard wear model, while the initial clearance and contact ellipse parameters are used to construct the potential contact state under load.

2.1.2. Loaded Tooth Contact Analysis for the Face Gear Pair

Based on the TCA results, the LTCA model shown in Figure 2 is established to determine the loaded contact state of the face gear pair. The theoretical contact trace is discretized into a series of potential contact points, and the deformation, clearance, and load at these points are solved simultaneously. For each potential contact point, the deformation compatibility condition is

$$u_i^{(1)} + u_i^{(2)} + \varepsilon_i - x_s - d_i = 0. \tag{3}$$

For all potential contact points at a given meshing position, the loaded contact equations can be written as

$$\begin{cases} -[\lambda]_{\text{Global}}\{F\} - \{u\}_{\text{Local}} + \{x_s\} + \{d\} = \{\varepsilon\}, \\ \sum_{i=1}^{N_c} F_i = P, \\ \text{if } F_i > 0,\ d_i = 0, \\ \text{if } F_i = 0,\ d_i > 0. \end{cases} \tag{4}$$

where $[\lambda]_{\text{Global}}$ is the global flexibility matrix obtained by the finite element substructure method, $\{u\}_{\text{Local}}$ denotes the local contact deformation, $\{F\}$ is the distributed load vector along the contact line, $\{x_s\}$ is the rigid-body approach vector applied to the potential contact points, $\{\varepsilon\}$ is the initial clearance vector, and $\{d\}$ is the residual clearance vector. The rigid-body approach x_s corresponds to the LTE along the normal line of action. The subscript i denotes the ith potential contact point, and N_c is the number of potential contact points at the current meshing position. These quantities correspond to the contact-line discretization, deformation compatibility, load distribution, and residual clearance illustrated in Figure 2.

The nonlinear contact equations are solved iteratively to obtain LTE and the load distribution. In the implementation, the TVMS at each meshing position is calculated by summing the pointwise ratios of the solved contact loads to their corresponding elastic approaches, after subtracting the initial local clearance:

$$k_m(\phi_j) = \sum_{i \in C_j} \frac{F_i(\phi_j)}{x_s(\phi_j) - \varepsilon_i(\phi_j)}, \qquad j = 1, 2, \ldots, M, \tag{5}$$

Here, C_j is the set of loaded contact points at meshing position ϕ_j, $F_i(\phi_j)$ is the solved normal load at point i, $x_s(\phi_j)$ is the loaded rigid-body approach, and $\varepsilon_i(\phi_j)$ is the initial local clearance used by the LTCA solver. The denominator therefore represents the elastic approach after removal of local gap closure. This implemented load-to-elastic-displacement aggregation is neither the global ratio P/x_s nor the slope of a load–displacement curve. The distributed load $\{F\}$ is also used in the subsequent contact-stress calculation. Thus, Figure 2 summarizes the LTCA procedure used in this study: the TCA-based potential contact points are taken as the input, the loaded contact state is obtained by enforcing deformation compatibility and load equilibrium, and the resulting load distribution and loaded approach are used to calculate contact stress, LTE, and TVMS.

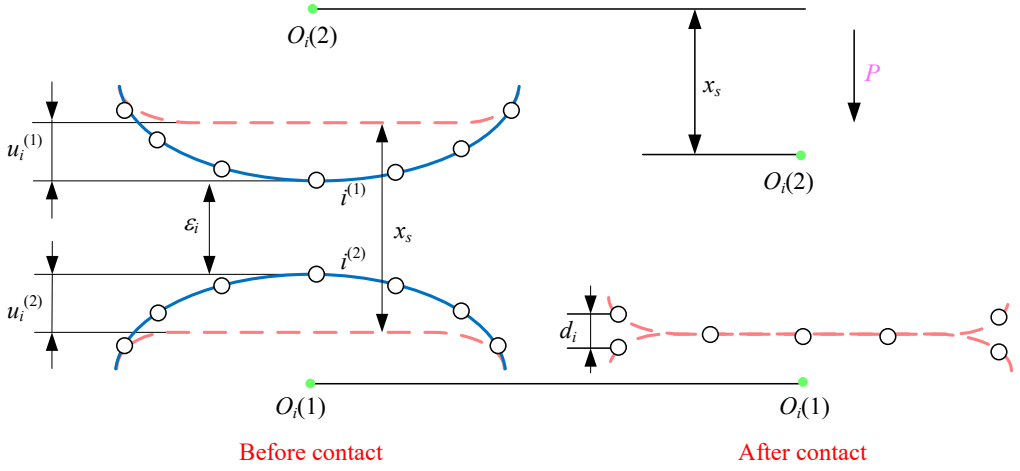


Figure 2. LTCA model of the face gear pair, showing the discretized potential contact points, deformation compatibility, load distribution, and residual clearance along the meshing path.

2.1.3. Contact Stress Calculation

The contact stress at each discrete contact point is calculated using Hertz contact theory. The equivalent elastic modulus is

$$\frac{1}{E_e} = \frac{1-\nu_p^2}{E_p} + \frac{1-\nu_f^2}{E_f}. \tag{6}$$

The second-order paraboloid parameters are obtained from the principal curvatures as

$$\begin{cases} A + B = \dfrac{1}{2}\left(\kappa_{p1} + \kappa_{p2} + \kappa_{f1} + \kappa_{f2}\right), \\ B - A = \dfrac{1}{2}\left[(\kappa_{p1} - \kappa_{p2})^2 + 2(\kappa_{p1} - \kappa_{p2})(\kappa_{f1} - \kappa_{f2})\cos 2\psi + (\kappa_{f1} - \kappa_{f2})^2\right]^{1/2}. \end{cases} \tag{7}$$

where κ_{pi} $(i = 1, 2)$ are the principal curvatures of the pinion tooth surface, κ_{fi} $(i = 1, 2)$ are the principal curvatures of the face gear tooth surface, and ψ is the angle between the two principal directions. The eccentricity of the contact ellipse is obtained from

$$\left(1 + \frac{A}{B}\right)(1 - e_h^2)\frac{K(e_h)}{E(e_h)} + e_h^2 - \frac{A}{B} - 1 = 0, \tag{8}$$

where $K(e_h)$ and $E(e_h)$ are complete elliptic integrals of the first and second kind, respectively. The auxiliary coefficients of the contact ellipse are

$$k_a = \left[\frac{2E(e_h)}{\pi(1 - e_h^2)}\right]^{1/3}, \qquad k_b = k_a(1 - e_h^2)^{1/2}. \tag{9}$$

Thus, the semi-major and semi-minor axes of the contact ellipse are

$$a_h = k_a\left[\frac{3F}{2E_e(A + B)}\right]^{1/3}, \qquad b_h = k_b\left[\frac{3F}{2E_e(A + B)}\right]^{1/3}, \tag{10}$$

where F is the local distributed load obtained from LTCA. After the contact ellipse parameters are obtained, the maximum contact stress is calculated as

$$P_{\max} = \frac{3F}{2\pi a_h b_h}. \tag{11}$$

2.1.4. Wear Depth Calculation

The wear depth is calculated by combining Hertz contact theory with Archard wear theory. At each discrete contact location, the sliding distance during a local contact passage is evaluated from the magnitude of the relative sliding velocity as

$$s_i = v\Delta t_i, \qquad i = p,f. \tag{12}$$

The subscripts p and f denote the pinion and face gear, respectively. Their local passage times are $\Delta t_p = 2b_h/V_p$ and $\Delta t_f = 2b_h/V_f$, using the corresponding surface speeds $V_p = \omega_p r_p$ and $V_f = \omega_f r_f$. Here, r_p and r_f are the distances of the TCA contact points from the respective rotation axes, and $\omega_f = \omega_p z_p/z_f$. The full contact width $2b_h$ is used for both members, while the relative sliding speed is evaluated as $v = |V_p - V_f|$. Thus, each member has its own sliding distance per loading event. The pinion and face-gear wear depths, h_p and h_g, are calculated separately as

$$\begin{aligned} h_p &= N_{w,p}k_p P_{\max} s_p = \frac{3N_{w,p}k_p F s_p}{2\pi a_h b_h}, \\ h_g &= N_{w,f}k_f P_{\max} s_f = \frac{3N_{w,f}k_f F s_f}{2\pi a_h b_h}, \end{aligned} \tag{13}$$

where k_p and k_f are the corresponding wear coefficients, and $N_{w,p}$ and $N_{w,f}$ are the respective loading-cycle counts per tooth. F is the distributed load at the discrete point on the contact line obtained from LTCA, and a_h and b_h are the semi-major and semi-minor axes of the contact ellipse. In the numerical implementation, the calculated wear depth is converted to micrometers for accumulation and visualization. Here, k_i is a dimensional effective coefficient in mm^2/N, and $P_{\max}$ is used as the representative pressure at each discrete contact location. This approximation uses the Hertzian peak pressure and does not separately integrate the pressure distribution over the contact ellipse. The coefficients are therefore interpreted together with this pressure approximation and the specified experimental conditions.

The cumulative wear is incorporated through contact-gap updates. Within each update batch, the LTCA load distribution and contact pressure are retained while the number of tooth-loading cycles is advanced. Under the present wear coefficients and operating conditions, the pinion has the larger wear increment and is therefore used to monitor the update threshold. Let Δh_p denote the incremental pinion wear field calculated for a candidate batch. The batch reaches the threshold when at least one discrete point satisfies $\Delta h_p \geq h_{\mathrm{th}}$, equivalently $\max(\Delta h_p) \geq h_{\mathrm{th}}$, where $h_{\mathrm{th}} = 2$ μm. If this condition is met, or if the prescribed total number of cycles is reached, the pinion and face-gear wear increments are accumulated and added to the current contact gap, after which the LTCA and pressure calculations are repeated. If neither condition is met, the candidate batch size is increased, and the wear increment is evaluated again. The face-gear wear increment is accumulated concurrently; it is not omitted from the gap update. Thus, the cycle count per update varies with the calculated wear rate, and the final batch is limited by the remaining prescribed cycles. The nominal TCA contact path and local curvatures are retained in this gap-update approximation. Using the pinion as the threshold-monitoring component is specific to the present case, in which its wear increment is larger; this choice is not intended as a universal criterion for other face-gear systems.

The sensitivity to the wear-update threshold was checked for the 22 N·m numerical condition with $N_{w,p} = 103,680$ loading cycles per pinion tooth. Thresholds of 2, 1, and 0.5 μm required 51, 102, and 203 updates, respectively. At the 2 μm threshold, the batch size ranged from 1277 to 2097 pinion-tooth loading cycles. Taking the 0.5 μm solution as the reference, the relative L_2 differences of the final pinion wear field, face-gear wear field, TVMS, and LTE obtained with 2 μm were 0.00749%, 0.00746%, 0.00241%, and 0.00648%,

respectively. Each difference is calculated as $100\|\boldsymbol{u}_2 - \boldsymbol{u}_{0.5}\|_2/\|\boldsymbol{u}_{0.5}\|_2$, where $\boldsymbol{u}$ contains all discrete values of the corresponding quantity and its subscript denotes the update threshold in micrometers. These small differences support the selected 2 μm threshold for this wear calculation within the contact-gap update approximation.

The cycle counts refer to loading events for each tooth rather than to the number of numerical updates. For an operating duration t_w in minutes and rotational speeds n_p and n_f in rpm, the counts are $N_{w,p} = n_p t_w$ and $N_{w,f} = n_f t_w = N_{w,p} z_p / z_f$. With $z_p = 23$ and $z_f = 276$, the face-gear count is one twelfth of the pinion count; these separate counts are used to calculate h_p and h_g, including within each wear-update batch. The worn meshing characteristics used in Section 2.2 are extracted after the prescribed wear calculation is completed.

2.2. Coupled Wear–Dynamics Modeling Framework

This section establishes the coupling between the wear-contact analysis and the nonlinear dynamic model. The worn tooth surface obtained in Section 2.1 is not introduced directly into the dynamic governing equations. Instead, it is first used to update the worn meshing characteristics, including TVMS, LTE, and wear-induced backlash. These phase-dependent meshing quantities are then used as inputs to the nonlinear dynamic model. Compared with conventional scalar backlash models, the proposed phase-dependent backlash model preserves the effect of nonuniform wear along the meshing path and therefore describes the time-varying backlash threshold that governs contact loss and re-engagement.

2.2.1. Overall Computational Procedure

As shown in Figure 3, the proposed method starts with the basic face gear parameters and the TCA results. The initial wear depth is set to zero, and the contact-line load distribution is then solved by LTCA. Based on the local load and sliding distance, the wear depth of the pinion and face gear is calculated using Archard's wear model. The accumulated material removal is incorporated into the tooth-surface clearance, and the worn clearance is updated iteratively until the prescribed number of wear cycles is reached. After the wear calculation is completed, LTCA is performed again using the wear-updated tooth-surface clearance to extract the worn TVMS, LTE, and backlash. These meshing quantities are finally introduced into the nonlinear dynamic model to obtain the time-domain response, frequency spectrum, phase portrait, and Poincaré section.

2.2.2. Calculation of Worn Meshing Characteristics

After each wear update, the tooth-surface geometry is updated according to the accumulated wear depth. Based on the updated surface geometry, LTCA is carried out to obtain the worn meshing characteristics. Since material removal changes the local contact boundary and the clearance between the mating tooth surfaces, the worn meshing characteristics are expressed as phase-dependent functions, namely $k_m = k_m(\phi)$, $e_{\mathrm{LTE}} = e(\phi)$, and $H = H(\phi)$, where $k_m(\phi)$ is the worn TVMS, $e(\phi)$ is the LTE, and $H(\phi)$ is the combined normal recession of the two working flanks. These quantities provide the main time-varying inputs to the nonlinear dynamic model. In the present implementation, the LTE fluctuation is used as the displacement excitation because the constant offset of LTE does not contribute to the dynamic excitation after differentiation.

Let $e_u(\phi)$ and $e_w(\phi)$ denote the unworn and worn LTE, respectively, and define $\Delta e_{\mathrm{LTE}}(\phi) = e_w(\phi) - e_u(\phi)$. The total recession of the two working flanks is $H(\phi) = h_p(\phi) + h_g(\phi)$. Let q_n be the dimensional relative normal coordinate referenced to the unworn LTE, and let $\delta_n = q_n - e_w(\phi)$ be the LTE-referenced coordinate used for contact; the dynamic state is $\Delta_n = \delta_n / b_c$. With the positive-torque convention used here, the positive

threshold is the drive-side working boundary. In the q_n coordinate, single-sided working-flank wear gives the worn boundaries $q_{+,w} = e_u + b_0 + H$ and $q_{-,w} = e_u - b_0$: the working-side boundary moves by H, while the back-side boundary remains fixed. Transforming to the LTE-referenced coordinate gives

$$\delta_+(\phi) = b_0 + H(\phi) - \Delta e_{\mathrm{LTE}}(\phi), \qquad \delta_-(\phi) = -b_0 - \Delta e_{\mathrm{LTE}}(\phi). \tag{14}$$

The separation is $\delta_+ - \delta_- = 2b_0 + H$, as required by the total clearance increase. The common $-\Delta e_{\mathrm{LTE}}$ term in the transformed bounds reflects the change of coordinate origin; it does not move the physical back-side boundary in the q_n coordinate. Thus, the wear recession enters the physical contact geometry once, through H at the working-side boundary. The varying worn LTE remains the excitation in the dynamic equation through its second derivative. The coordinate transformation and boundary positions are illustrated in Figure 4.

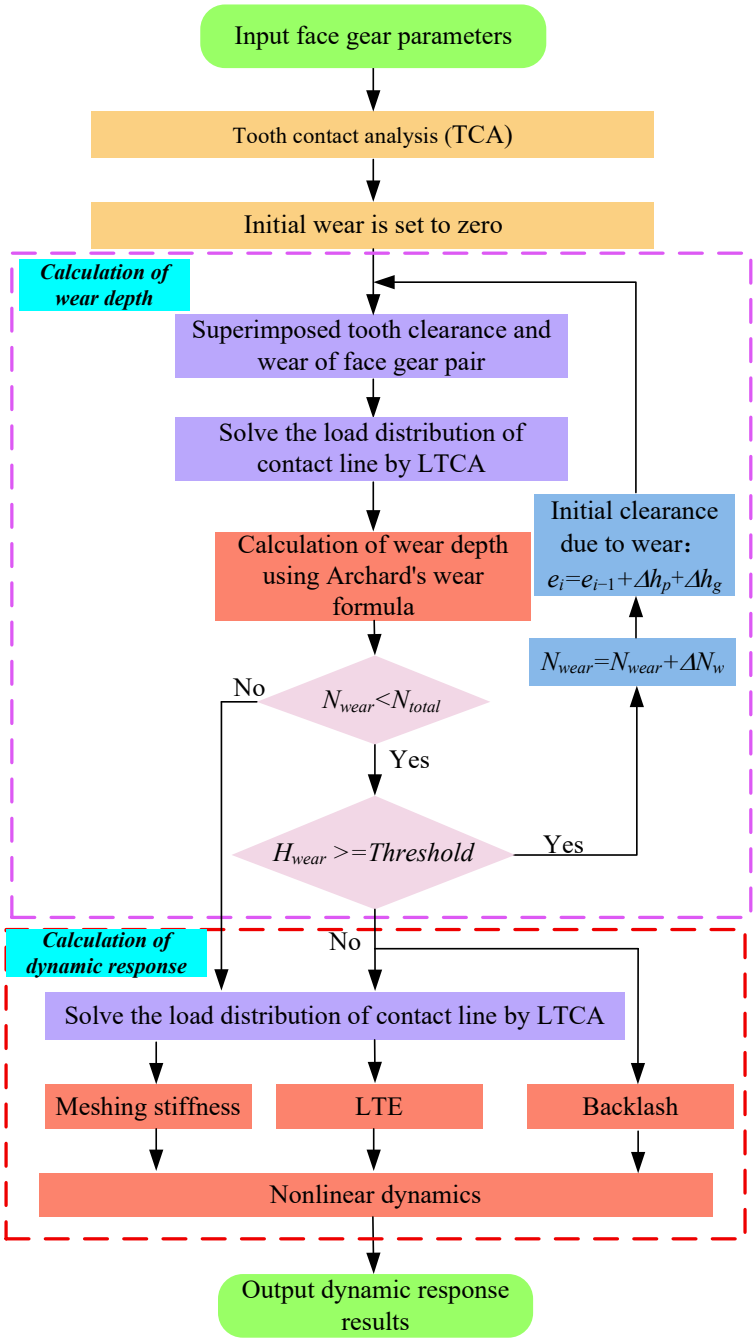


Figure 3. Computational procedure of the coupled wear–dynamics framework.

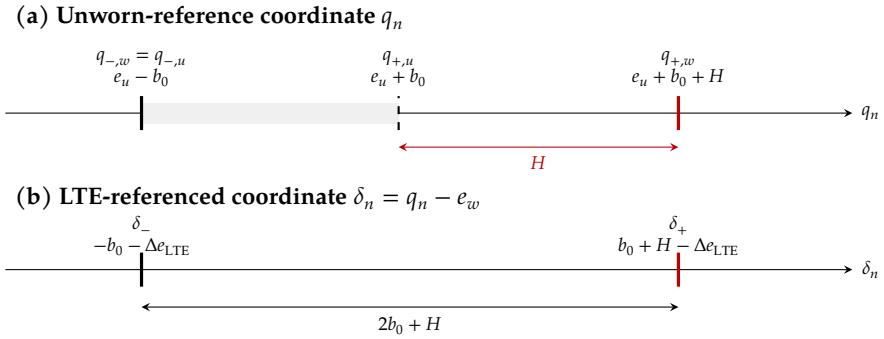


Figure 4. Schematic of the single-sided working-flank wear boundaries (not to scale). In q_n, wear shifts only the working-side boundary by H; transforming to the LTE-referenced coordinate shifts both threshold coordinates by $-\Delta e_{\mathrm{LTE}}$, while preserving the total clearance width.

The normal-direction wear depths are obtained from the accumulated pinion and face-gear wear fields. Their combined surface recession satisfies $H(\phi) = h_p(\phi) + h_g(\phi) \approx \Delta \boldsymbol{r}_w(\phi) \cdot \boldsymbol{n}(\phi)$, where $\Delta \boldsymbol{r}_w(\phi)$ is the combined recession vector and $\boldsymbol{n}(\phi)$ is the local mesh normal. For descriptive plots of the clearance increase, the corresponding half-width increment is $H(\phi)/2$; it is not used as a symmetric contact threshold in the present model. The existing spatial averaging and LTCA meshing-position grouping are retained when reducing these wear fields to scalar values or phase-dependent nodes.

For spatial consistency, the wear values used to construct $H(\phi)$ and the LTE-referenced boundaries are first grouped according to the LTCA meshing-position mapping. The contact-line rows in the wear arrays are aggregated using the mapping returned by LTCA (ten meshing positions in the present calculation), rather than being mapped directly, row by row, to equally spaced phase nodes. The resulting phase table and LTE samples use the same meshing-phase coordinate while retaining the distinct geometric and excitation roles described above.

The contact ratio is prescribed as 1.7. During dynamic integration, the phase is evaluated as $\phi(t) = \mathrm{mod}(\omega_m t, 2\pi) = \mathrm{mod}(W\tau, 2\pi)$. The same phase-dependent parameter functions are repeated in each mesh period, corresponding to an assumption of identical wear among the teeth.

2.2.3. Wear-Induced Backlash Modeling

Four descriptions of the wear-induced clearance increase are compared: Minimum, Full-field mean, Phase average, and Phase-dependent. The half-width increment is denoted by $\Delta b(\phi) = H(\phi)/2$. The first three descriptions replace $H(\phi)$ by a constant, while the phase-dependent description retains its variation over a mesh period. All four use the same asymmetric working-side and back-side boundary formulation; the scalar descriptions do not redistribute working-flank wear to the back side.

In the minimum model, the minimum wear-induced backlash increment within one mesh cycle is used as the equivalent scalar value:

$$\begin{aligned} \Delta b_{\min} &= \min_{\phi} \Delta b(\phi), \\ b_{\min} &= b_0 + \Delta b_{\min}. \end{aligned} \tag{15}$$

Here, $b_{\min}$ describes half the total clearance width. The corresponding working-side recession input is $H_{\min} = 2\Delta b_{\min}$; it is not a symmetric contact threshold.

In the Full-field mean model, the half-width increment is obtained from the arithmetic spatial average of all entries in the stored pinion and face-gear wear fields:

$$\begin{aligned} \Delta b_{\text{mean}} &= \frac{1}{2n_\ell n_q} \sum_{\ell=1}^{n_\ell} \sum_{q=1}^{n_q} \left(h_{p,\ell q} + h_{g,\ell q} \right), \\ b_{\text{mean}} &= b_0 + \Delta b_{\text{mean}}, \end{aligned} \tag{16}$$

where n_ℓ is the number of contact-line rows, n_q is the number of discrete points per row, and $h_{p,\ell q}$ and $h_{g,\ell q}$ are the accumulated normal wear depths of the two working flanks at the corresponding stored locations. All depths are expressed in the same length units as b_0. Each stored point has equal weight in this full-field average; it is distinct from an average of the grouped phase nodes or an integral over the meshing phase.

The Phase average model uses the integral mean of the periodic interpolation employed by the dynamic solver:

$$\overline{\Delta b}_\phi = \frac{1}{2\pi} \int_0^{2\pi} \Delta b_{\text{interp}}(\phi)\, d\phi.$$

For the present wear field, the full-field mean is 52.1655 µm, the ten-node arithmetic mean is 47.1584 µm, and the periodic PCHIP integral mean is 47.0843 µm. The full-field mean includes all 15 stored rows, whereas the phase function uses ten retained phase groups. The additional five stored rows have a larger mean half-width increment of 62.1796 µm, explaining the higher full-field mean. The stored wear field spans contact positions over the wear history rather than representing one instantaneous contact set.

For each scalar description j, set $H_j = 2\Delta b_j$ and use $\delta_{+,j}(\phi) = b_0 + H_j - \Delta e_{\text{LTE}}(\phi)$ and $\delta_{-j}(\phi) = -b_0 - \Delta e_{\text{LTE}}(\phi)$. The same worn TVMS, LTE, and coordinate shift are retained in all four comparisons. In particular, the Phase average and Phase-dependent descriptions have the same period-averaged clearance width, so their difference isolates the effect of the phase variation of H.

2.2.4. Phase-Dependent Backlash Model

Nonuniform tooth surface wear leads to different amounts of material removal at different meshing phases, resulting in phase-dependent variations in the contact boundary and backlash. During operation, the meshing phase evolves with time; the working-side and back-side boundaries used in the dynamic model are therefore

$$\begin{aligned} \delta_+(\phi(t)) &= b_0 + H(\phi(t)) - \Delta e_{\text{LTE}}(\phi(t)), \\ \delta_-(\phi(t)) &= -b_0 - \Delta e_{\text{LTE}}(\phi(t)), \\ \delta_+(\phi(t)) - \delta_-(\phi(t)) &= 2b_0 + H(\phi(t)). \end{aligned} \tag{17}$$

Here, b_0 is the initial half-backlash, $H = h_p + h_g$ is the combined recession of the two working flanks, and $\Delta e_{\text{LTE}} = e_w - e_u$. The quantities δ_+ and δ_- are dimensional thresholds in the LTE-referenced coordinate. Their difference gives the total clearance width, while the back-side boundary remains fixed in the unworn-reference coordinate as shown in Equation (14).

2.3. Nonlinear Dynamic Model of the Worn Face Gear Pair

In this section, the phase-dependent TVMS, LTE, and backlash obtained from the coupled framework are introduced into the nonlinear dynamic model. In the numerical implementation, a reduced five-degree-of-freedom dynamic model is used. The state variables consist of the dimensionless translational displacements of the pinion and face gear in the mesh plane and the dimensionless relative displacement along the mesh normal direction. The omission of the pinion axial coordinate is based on the ideal spur-type pinion configuration: the nominal mesh force has no component along the pinion axis, so

its axial displacement and associated support are excluded. Peng and Zhou adopted this simplification in a face-gear model retaining the six coordinates $\{x_1, y_1, x_2, y_2, \theta_1, \theta_2\}^{\mathrm{T}}$ [37]. Here, the two rotational coordinates are represented through the relative mesh displacement, giving the five coordinates used below. The zero-axial-force statement refers specifically to the pinion axis; the translational coordinates of the projected model remain distinct from a complete three-dimensional gear–shaft description.

2.3.1. Nondimensional Dynamic Parameters and Meshing Excitations

Let the displacement scale be $b_c = 1$ μm, and let the dimensionless time be $\tau = \omega_n t$, where $\omega_n = \sqrt{k_{\mathrm{mean}}/m_e}$ and $m_e = J_1 J_2/(J_1 r_2^2 + J_2 r_1^2)$. Here, k_{mean} is the mean mesh stiffness obtained from LTCA, J_1 and J_2 are the rotational inertias, and r_1 and r_2 are the pitch radii of the pinion and face gear. The mass m_e is the rotational reduced mass associated with the pitch-coordinate displacement $r_1\theta_1 - r_2\theta_2$. The frequency ω_n is used as a reference scale for nondimensionalization. The dimensionless generalized coordinate vector is $\boldsymbol{q} = \{X_1, Y_1, X_2, Y_2, \Delta_n\}^{\mathrm{T}}$, where X_1, Y_1 and X_2, Y_2 are the dimensionless translational displacements of the two gears, and Δ_n is the dimensionless relative displacement along the mesh normal direction. The corresponding dimensional displacement is recovered as $x = b_c X$.

The mesh angular frequency is $\omega_m = 2\pi n_1 z_1/60$, and the dimensionless excitation frequency is $W = \omega_m/\omega_n$. The TVMS and LTE are represented by Fourier series fitted to the LTCA results:

$$\begin{aligned} k_m(\tau) &= a_0^{(k)} + \sum_{j=1}^{N_F}\left[a_j^{(k)}\cos(jW\tau) + b_j^{(k)}\sin(jW\tau)\right], \\ e(\tau) &= a_0^{(e)} + \sum_{j=1}^{N_F}\left[a_j^{(e)}\cos(jW\tau) + b_j^{(e)}\sin(jW\tau)\right]. \end{aligned} \tag{18}$$

In the dynamic equation, LTE enters through its second derivative with respect to dimensionless time.

2.3.2. Nonlinear Backlash Function

The backlash function uses two dimensionless thresholds, $D_+(\tau) = \delta_+(\phi(t))/b_c$ and $D_-(\tau) = \delta_-(\phi(t))/b_c$. All four backlash descriptions use Equation (17); the scalar cases replace $H(\phi)$ by $H_j = 2\Delta b_j$ while retaining the same LTE coordinate shift. The two thresholds are constructed at the ten phase nodes and interpolated separately using PCHIP with periodic closure. Thus, a scalar clearance width does not remove the time dependence associated with the common LTE reference. The resulting backlash nonlinearity is

$$f_b(\Delta_n, \tau) = \begin{cases} \Delta_n - D_+(\tau), & \Delta_n > D_+(\tau), \\ 0, & D_-(\tau) \le \Delta_n \le D_+(\tau), \\ \Delta_n - D_-(\tau), & \Delta_n < D_-(\tau). \end{cases} \tag{19}$$

In the numerical examples of this study, the support clearance is set to zero. Therefore, the bearing supports are modeled as linear stiffness–damping elements, and no additional support-clearance nonlinearity is introduced.

2.3.3. Mesh Force and Friction Force

The dimensional dynamic mesh force is written as

$$F_\delta = \begin{cases} k_m(\tau) b_c f_b(\Delta_n, \tau) + c_m b_c \omega_n \dot{\Delta}_n, & f_b \neq 0, \\ 0, & f_b = 0, \end{cases} \tag{20}$$

where $c_m = 2\zeta\sqrt{k_{\text{mean}} m_e}$ is the mesh damping coefficient and the dot denotes differentiation with respect to τ. Here, ζ specifies the damping coefficient using the reference mass m_e. When friction is included, the friction force is written as $F_f = \mu F_\delta \gamma_s$, where μ is the friction coefficient and $\gamma_s = \text{sgn}(v_s)$ is determined by the equivalent sliding velocity along the line of action. In the implementation, $v_s = L_{12}\omega_1 - L_{21}\omega_2$, where L_{12} and L_{21} are the instantaneous equivalent lever arms from the two gears to the contact point.

2.3.4. Dimensionless Equations of Motion

Let $u_n = (x_1 - x_2)\cos\alpha + (y_1 - y_2)\sin\alpha$ denote the translational contribution to the normal relative displacement. The dimensional coordinate and the two torque balances are

$$\begin{aligned} \delta_n = b_c\Delta_n &= (r_1\theta_1 - r_2\theta_2)\cos\alpha + u_n - e(t), \\ J_1\ddot{\theta}_1 &= T_1 - r_1\cos\alpha\, F_\delta - \ell_1 F_f, \\ J_2\ddot{\theta}_2 &= r_2\cos\alpha\, F_\delta + \ell_2 F_f - T_2. \end{aligned}$$

The angular accelerations in these dimensional balances are derivatives with respect to t, and the nominal output torque is $T_2 = T_1 r_2/r_1$. The normal-force moment arms are $r_i\cos\alpha$, consistent with the displacement projection. One factor of $\cos\alpha$ enters through the moment arm and the other through the rotational displacement projection. Eliminating the angular accelerations therefore gives the reaction term $-F_\delta\cos^2\alpha/m_e$. At static torque balance, $F_{\delta,0} = T_1/(r_1\cos\alpha)$; for $T_1 = 22$ N·m, $r_1 = 0.0253$ m, and $\alpha = 20°$, this gives 925.37 N. The corresponding rotational reduced mass in the normal coordinate is $m_e/\cos^2\alpha$. By projecting the mesh force, friction force, and support restoring forces onto the translational directions, the dimensionless equations of motion are written as

$$\begin{cases} \ddot{X}_1 = \dfrac{-F_\delta\cos\alpha - F_f\sin\alpha - F_{b1x}}{m_1 b_c\omega_n^2}, \\ \ddot{Y}_1 = \dfrac{-F_\delta\sin\alpha + F_f\cos\alpha - F_{b1y}}{m_1 b_c\omega_n^2}, \\ \ddot{X}_2 = \dfrac{F_\delta\cos\alpha + F_f\sin\alpha - F_{b2x}}{m_2 b_c\omega_n^2}, \\ \ddot{Y}_2 = \dfrac{F_\delta\sin\alpha - F_f\cos\alpha - F_{b2y}}{m_2 b_c\omega_n^2}, \\ \ddot{\Delta}_n = \dfrac{F_t\cos\alpha}{m_e b_c\omega_n^2} - \dfrac{F_\delta\cos^2\alpha}{m_e b_c\omega_n^2} - \dfrac{m_f F_f\cos\alpha}{m_e b_c\omega_n^2} \\ \qquad\quad + (\ddot{X}_1 - \ddot{X}_2)\cos\alpha + (\ddot{Y}_1 - \ddot{Y}_2)\sin\alpha - \dfrac{\ddot{e}}{b_c}. \end{cases} \tag{21}$$

Here, F_{bij} denotes the linear support restoring force of gear i in the j direction ($j = x, y$), including the corresponding stiffness and damping contributions. The support stiffnesses are $k_{1x} = k_{1y} = 2.0\times10^8$ N/m and $k_{2x} = k_{2y} = 5.0\times10^8$ N/m, while the damping coefficients are $c_{1x} = c_{1y} = 2.0\times10^4$ N s/m and $c_{2x} = c_{2y} = 5.0\times10^4$ N s/m. The nominal tangential load is $F_t = T_1/r_1$. The dimensionless friction-coupling factor used in the implementation is $m_f = (r_1\ell_1 J_2 + r_2\ell_2 J_1)/(J_1 r_2^2 + J_2 r_1^2)$, with $\ell_i = r_i\sin\alpha$; this gives $m_f = \sin\alpha$ for the prescribed equivalent lever arms. All dots in the nondimensional equations denote derivatives with respect to τ, including $\ddot{e} = d^2e/d\tau^2$, where e retains dimensional displacement units. The governing equations are solved by numerical time integration.

2.3.5. Numerical Solution and Response Indicators

Each parameter point is integrated independently using the ode45 solver in MATLAB R2025a with relative and absolute tolerances of 10^{-8}. After the transient portion is discarded,

the response is sampled once per mesh period at $t_n = t_0 + nT_m$, where $T_m = 60/(n_1 z_1)$. The displacement spread of the sampled points is quantified by the Poincaré displacement span

$$S_p = \max_n[x_p(n)] - \min_n[x_p(n)], \tag{22}$$

where $x_p(n)$ is the displacement at the nth Poincaré point and S_p is expressed in micrometers. Because S_p is based only on displacement, it cannot identify the response period by itself; a large value also does not imply chaotic motion or dynamic instability. The velocity corresponding to each displacement sample is retained, so that a Poincaré point is represented by $(x_p(n), v_p(n))$. Here, v_p denotes the physical relative mesh-normal velocity, $v_n = b_c\omega_n\dot{\Delta}_n$, expressed in m/s; it is the time derivative of the relative normal displacement used by the contact law, rather than the tangential sliding velocity used in the wear calculation. Periodicity is assessed by comparing paired points separated by integer mesh-period lags, and recurrent clusters are counted in the displacement–velocity plane. The span is therefore used for response screening, whereas period identification is based on the paired samples.

The global and refined scans use 150 mesh periods; after the first half is discarded, 76 paired Poincaré samples are retained. The representative cases are integrated for 2000 mesh periods, and paired samples and response statistics are also evaluated in successive 200-period windows to check for slow transients. Four initial-condition pairs are examined. Writing $\Delta_n(0) = a_0 - e(0)/b_c$ and $\dot{\Delta}_n(0) = v_0 - e'(0)/b_c$, the prescribed dimensionless pairs (a_0, v_0) are $(0.05, 0.01)$, $(0, 0)$, $(50, 1)$, and $(-50, -1)$, with the other initial displacements and velocities set to zero. The representative response plots use the first pair and the final 80 mesh periods. Each backlash description in the clearance sweep is also evaluated independently from all four pairs for 2000 mesh periods; the final state at one clearance is not passed to the next. The final 80 paired samples are used for the Poincaré analysis and the final 80 periods for the response statistics. When cases have different mean mesh stiffnesses, the physical input speed and physical initial velocity are held fixed; the latter is specified using the common worn-system reference scale, $v_0 b_c \omega_{n,w}$. The sampling phase is fixed at 0.9875 of a mesh period for all parameter points. These mesh-period counts refer to the dynamic calculation and are distinct from the tooth-loading cycles used in the wear calculation.

For P1, the correlation form of the 0–1 test [38] is additionally applied to the final 1600 stroboscopic displacement samples, with one sample per mesh period. The test uses 100 values of c distributed over $(\pi/5, 4\pi/5)$ and a maximum lag of one tenth of the sample length; the reported K is their median correlation coefficient. The final 1000 samples are also tested to check sensitivity to the observation length.

For the damping-sensitivity analysis, P1 and P2 ($W = 1.19$, $b_0 = 92.5$ and 70 μm, respectively) are each evaluated at $\zeta = 0.04$, 0.06, 0.08, 0.10, and 0.12. Only the mesh damping parameter is varied; the support damping, default initial condition, worn TVMS/LTE, and asymmetric contact boundaries are unchanged. An additional four-model comparison uses $W = 0.15$, $b_0 = 70$ μm, and $\zeta = 0.08$, for which the phase-dependent model has approximately 15% contact loss. Each case is integrated independently for 2000 mesh periods, with statistics calculated over the final 80 periods and periodicity checked in successive 200-period windows.

For the representative and model-comparison cases, integer lags of 1–64 mesh periods are examined. The smallest lag for which the repeated samples satisfy RMS tolerances of 0.001 μm in displacement and 10^{-4} m/s in velocity is taken as a candidate period, and the associated point clusters are counted. This procedure identifies periodicity at the adopted sampling precision; it is not a Lyapunov-based chaos test.

The phase fraction 0.9875 is a fixed numerical reference retained for consistency across parameter points, rather than a physically distinguished phase. To assess sensitivity to this

choice, the saved 2000-period trajectories for P1 and P2 were re-sampled at phase fractions of 0, 0.25, 0.50, 0.75, and 0.9875. At each phase, the same paired displacement–velocity period criterion was applied, and successive 200-period windows were checked to distinguish settled periodic responses from slowly evolving transients.

The equivalent lumped parameters used in the simulations are listed in Table 1. Initial translational displacements and velocities are set to zero, and the normalized relative coordinates are initialized as $\Delta_n(0) = 0.05 - e(0)/b_c$ and $\dot{\Delta}_n(0) = 0.01 - e'(0)/b_c$. The friction direction is determined from the sign of the equivalent sliding velocity. The masses and inertias are prescribed equivalent-disk parameters for the numerical model, calculated as $m_i = \rho\pi r_i^2 L_i$ and $J_i = m_i r_i^2/2$, using $L_1 = 22$ mm for the pinion-side equivalent thickness (taken as the 22 mm pinion tooth width), $L_2 = 60$ mm for the face-gear equivalent thickness, and $\rho = 7800$ kg/m^3. The face-gear tooth width is 18 mm; it is distinct from the prescribed equivalent thickness L_2. The actual face gear is not a uniform solid disk; the disk representation is a lumped numerical approximation, not a geometric reconstruction. The available prototype mass-property information was insufficiently documented to derive a verified, axis-specific equivalent parameter set for this dynamic model. Accordingly, $m_2 = 135.52$ kg and $J_2 = 6.246$ kg m^2 are prescribed modeling assumptions, not measured properties of the test gear. Since these quantities enter m_e, ω_n, and W, the reported dynamic responses are conditional on the prescribed values; transfer to a specific face-gear assembly requires verified mass properties.

Table 1. Equivalent dynamic-model parameters and numerical settings.

Parameter	Value	Unit
Equivalent pitch radii r_1, r_2	0.0253, 0.3036	m
Equivalent lumped masses m_1, m_2	0.34507, 135.51871	kg
Rotational inertias J_1, J_2	1.10438×10^{-4}, 6.24558	kg m^2
Mean mesh stiffness, unworn TVMS $k_{\mathrm{mean,u}}$	1.96633×10^8	N/m
Reference natural frequency, unworn TVMS $\omega_{n,u}$	3.38019×10^4	rad/s
Mean mesh stiffness, worn TVMS $k_{\mathrm{mean,w}}$	1.96453×10^8	N/m
Reference natural frequency, worn TVMS $\omega_{n,w}$	3.37864×10^4	rad/s
Reference mesh damping parameter ζ	0.08	–
Friction coefficient μ	0.02	–
Friction-coupling factor m_f	0.34202	–
Displacement scale b_c	1	µm
Fourier terms N_F	4	–
Nominal tangential load F_t at 22 N·m	869.565	N
Pinion support stiffness $k_{1x} = k_{1y}$	2.0×10^8	N/m
Face-gear support stiffness $k_{2x} = k_{2y}$	5.0×10^8	N/m
Pinion support damping $c_{1x} = c_{1y}$	2.0×10^4	N s/m
Face-gear support damping $c_{2x} = c_{2y}$	5.0×10^4	N s/m
Support clearance	0	µm
Time integrator	ode45	–
Relative/absolute tolerances	$10^{-8}/10^{-8}$	–

3. Results

3.1. Experimental Assessment

This section assesses the contact trace, calibrates effective wear coefficients using tooth-surface measurements, and compares the calculated and measured pinion wear distributions after calibration. The measured input torque is also used for a frequency-domain consistency

check. These assessments concern different parts of the framework and are distinguished below. The basic parameters of the tested face gear pair are shown in Table 2.

The wear experiment was conducted in a liquid medium rather than under conventional gear-oil conditions. The underlying tooth-surface measurements and torque records, material identity and restricted material parameters, heat-treatment information, surface roughness, and test-liquid identity cannot be disclosed because of project confidentiality requirements. These restrictions limit independent verification of the wear-coefficient calibration and experimental comparisons. The present model does not resolve the lubrication regime or the effects of the liquid medium.

The effective wear coefficients for the pinion and face gear are 3.5×10^{-7} and 2×10^{-6} mm^2/N, respectively, and were determined from wear measurements of the corresponding members. These coefficients are specific to the stated test conditions and Archard formulation; they should not be regarded as universal values or attributed solely to the liquid medium. The same measurements are used for coefficient calibration and profile comparison, so the latter is interpreted as a post-calibration comparison.

At the nominal speed of 23.3 rpm, the 21,600 min test corresponds to 503,280 pinion rotations, or 503,280 loading cycles per pinion tooth and 41,940 per face-gear tooth, using $z_p/z_f = 23/276$.

Table 2. Basic parameters of the tested face gear pair.

Parameter	Value	Unit
Number of teeth of pinion	23	–
Number of teeth of face gear	276	–
Number of teeth of shaping cutter	24	–
Module	2.2	mm
Pressure angle	20	°
Tooth width of pinion	22	mm
Tooth width of face gear	18	mm
Face gear inner radius	294.6	mm
Face gear outer radius	312.6	mm
Axis angle	90	°
Pinion wear coefficient	3.5×10^{-7}	mm^2/N
Face gear wear coefficient	2×10^{-6}	mm^2/N
Wear time	21,600	min
Speed of input shaft	23.3	rpm
Nominal input-shaft torque	2.2	N · m

3.1.1. Gear Rolling Test

A gear rolling test was conducted to assess the accuracy of the TCA model. A colorant was applied to the tooth surface, and the contact mark was obtained after the pinion and face gear meshed under the prescribed assembly condition. The experimentally observed contact area was then compared with the theoretical contact trace obtained from TCA.

As shown in Figure 5, the calculated contact trace is located near the central region of the tooth surface and agrees well with the measured contact mark. This indicates that the established TCA model can reasonably describe the actual meshing position of the face gear pair.

3.1.2. Tooth Surface Measurement

The tooth-surface measurements were performed with assistance from Qinchuan Machine Tool (Baoji, China) using its equipment. The experimental work was conducted

by the third author in collaboration with a research institute under a confidential project. Consequently, detailed source records and some test-specific material information cannot be released. The documentation available to the authors does not specify the numbers of measured teeth and profiles or a measurement-uncertainty estimate.

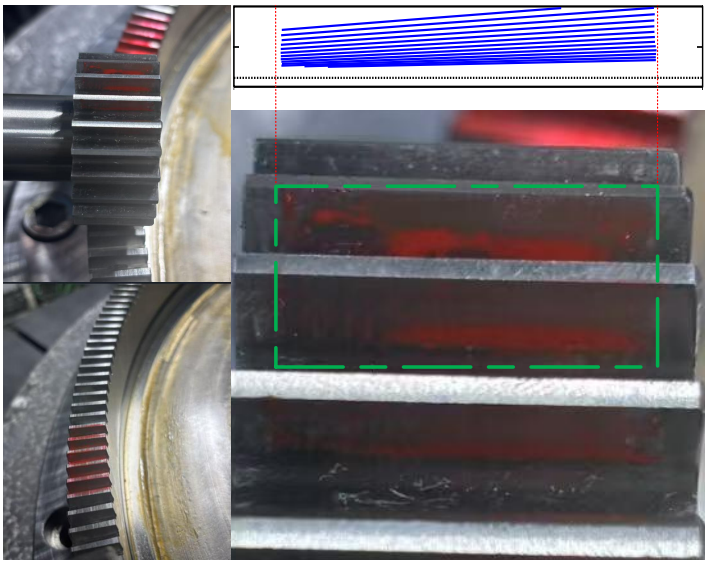


Figure 5. Comparison between the theoretical contact trace and the experimentally measured contact mark.

After the wear test, the tooth surface morphologies of both the pinion and face gear were measured to obtain the wear depth distribution. Measurements of the two members were used to calibrate their respective effective wear coefficients. The profile comparison presented here is limited to the pinion. As shown in Figure 6, the measured worn pinion tooth surface is presented. The measured pinion distribution is used to assess the calculated wear pattern after coefficient calibration. A corresponding quantitative face-gear profile comparison cannot be established from the retained records.

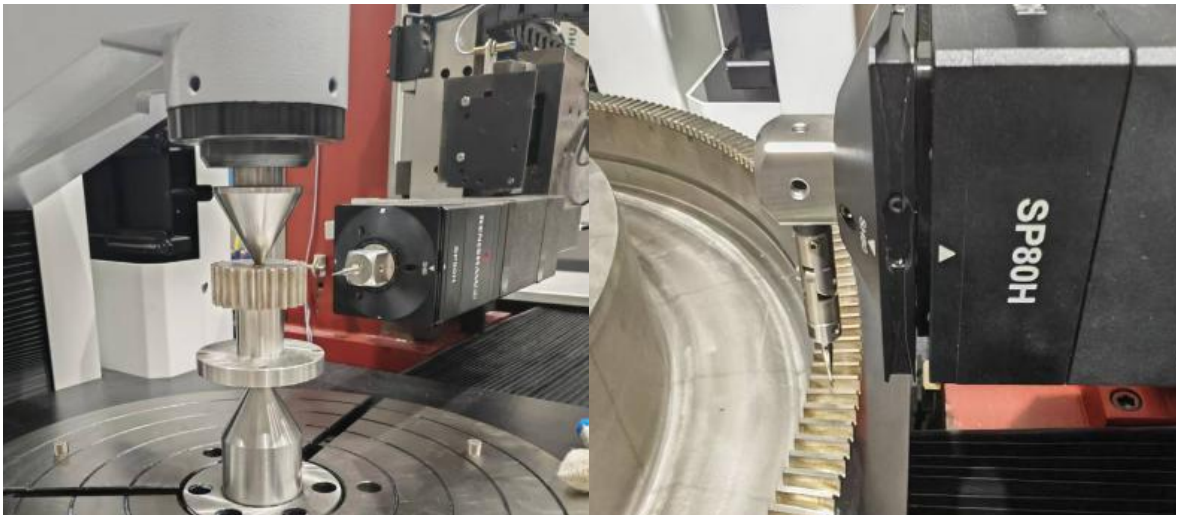
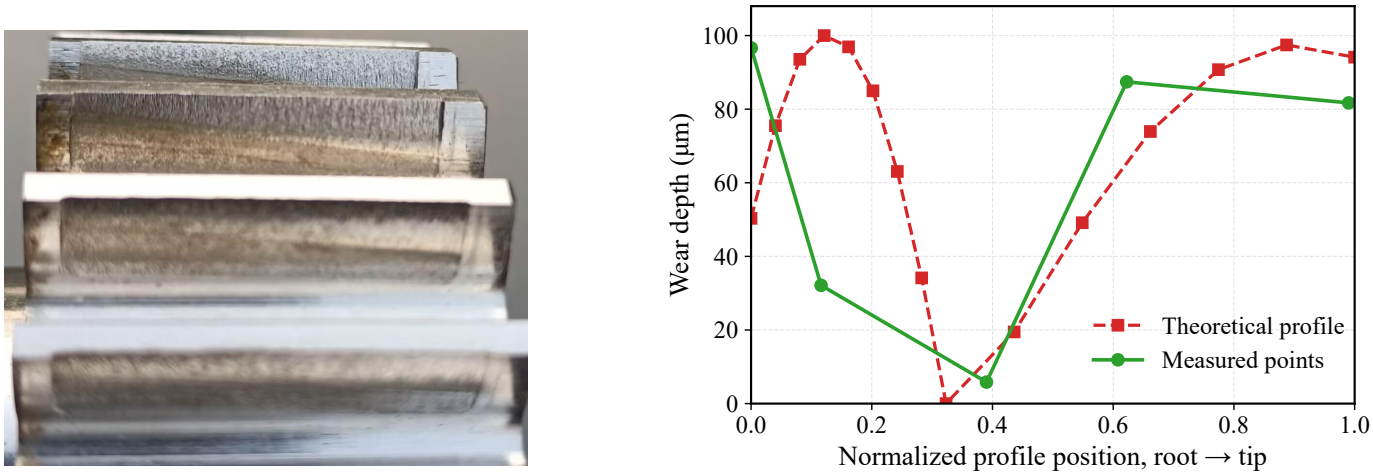


Figure 6. Tooth surface measurement of the worn pinion.

3.1.3. Wear-Coefficient Calibration and Wear-Profile Comparison

The calculated pinion wear depth is compared with the measurement-derived profile used to calibrate the effective wear coefficient. The profiles in Figure 7 both show lower

wear near the pitch region and higher wear away from it, but differ in local depth and the position of the minimum. The calculated maximum wear depth and the measured maximum reported for this comparison are approximately 100.0 µm and 96.6 µm, respectively. Their absolute difference is 3.36 µm, or 3.48% relative to the measured value. This difference refers only to the reported pair of maxima; it does not quantify error along the full profile or variability among measured teeth. The sampling coverage and selection of the reported measured maximum cannot be verified from the retained documentation. A verified point-wise correspondence for the plotted profiles cannot be established from these records, so a full-profile error statistic is not reported. Because the same tooth-surface measurements were used for coefficient calibration and this comparison, the result is a post-calibration comparison rather than an independent validation. The calibrated coefficients are used in the subsequent numerical wear-state and dynamic calculations.



(**a**) (**b**)

Figure 7. Pinion wear assessment after coefficient calibration: (**a**) photograph of the worn pinion tooth surface; (**b**) comparison between calculated and measured wear depths using the calibration dataset.

3.1.4. Kinematic Frequency Check Using Measured Input Torque

During the wear test, vibration signals and input torque were measured simultaneously. However, the test was conducted at a low rotational speed and a small input torque, and the measured vibration response was weak. The input torque signal is therefore used for a frequency-domain consistency check. Its mean is removed, and the fluctuating component is divided by the pinion pitch radius to obtain a torque-derived equivalent force. This is a system-level signal rather than a direct measurement of the local normal mesh force.

A 513.024 s segment sampled at 10 kHz was analyzed. Its mean torque is approximately 1.482 N·m, below the nominal test setting of 2.2 N·m in Table 2. The available records do not establish the cause of this difference. After removal of the mean and robust treatment of outliers, the torque-derived equivalent-force and simulated-force spectra were calculated using a Hann-windowed FFT over 6–22 Hz and normalized independently.

At 23.3 rpm with 23 pinion teeth, the kinematic mesh frequency is $f_m = n_1 z_1/60 =$ 8.932 Hz. The dominant measured peak at 8.904 Hz corresponds to a pinion speed of 23.228 rpm. This agreement checks the consistency of rotational speed and mesh frequency; it does not independently validate the dynamic model. The measured peak and its twice-frequency reference, approximately 17.808 Hz, are marked in Figure 8. The additional measured peaks near 12 and 17.5 Hz are absent from the simulation; the latter does not coincide with the twice-frequency reference. Their origins cannot be identified from the available input-torque record alone and are not assigned to specific gear-mesh harmonics or components.

Because the spectra are independently normalized, this comparison also does not establish agreement in absolute response amplitudes or dynamic loads, at either the tested low speed or higher speeds.

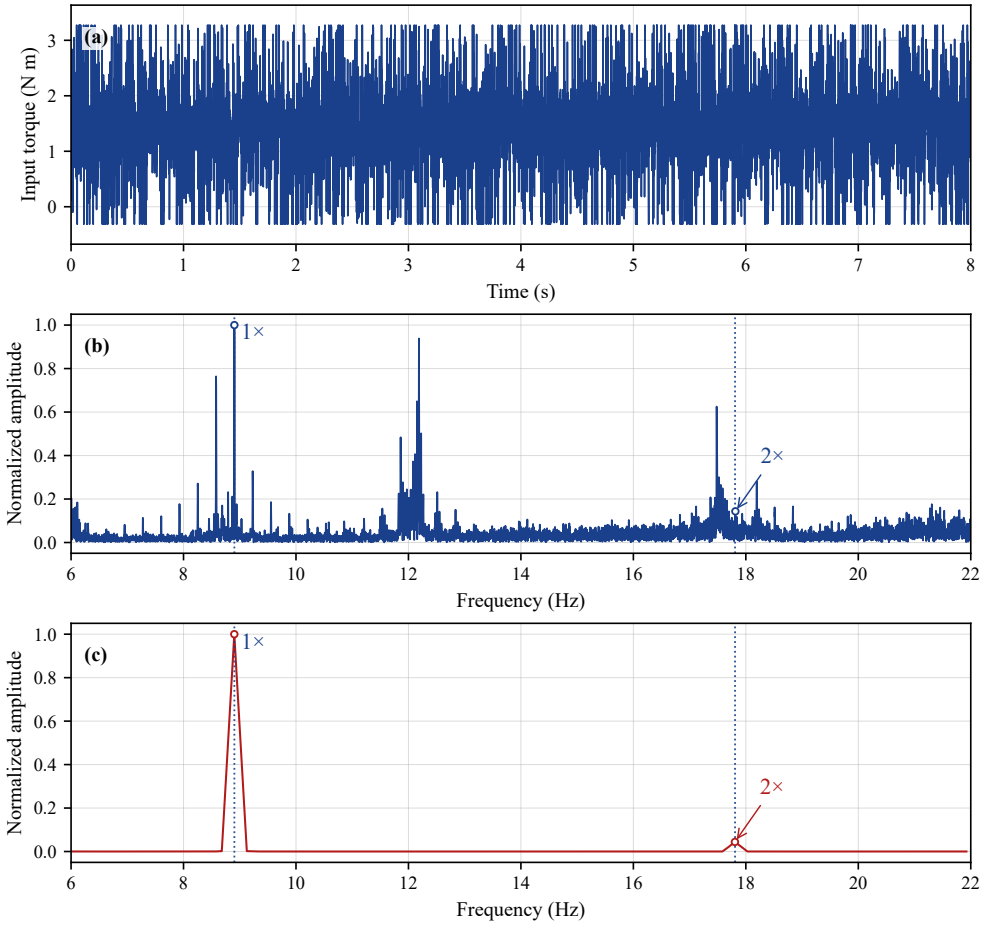


Figure 8. Torque-based kinematic frequency check under the tested low-speed condition: (**a**) measured input torque; (**b**) normalized spectrum of the torque-derived equivalent force; (**c**) normalized spectrum of the simulated dynamic mesh force. The identified mesh frequency and twice this frequency are marked as comparison references. Each spectrum is normalized independently.

3.2. Numerical Results

The numerical calculations use the effective wear coefficients identified in Section 3.1. To investigate the dynamics at higher operating speeds while retaining a wear severity comparable to that observed experimentally, the accumulated loading-cycle count was adjusted in the numerical wear calculation. At the prescribed reference condition of 22 N·m and 14,000 rpm, $N_{w,p} = 103,680$ loading cycles per pinion tooth and $N_{w,f} = 8640$ cycles per face-gear tooth give a maximum pinion wear depth of approximately 99.8 µm, close to the reported experimental value of 96.6 µm. The resulting geometry defines a prescribed severe-wear reference state for the dynamic analysis.

This prescribed state is distinct from the experimental wear test, which was conducted at 2.2 N·m and 23.3 rpm for 21,600 min (Table 2). The low-speed-calibrated coefficients are retained as numerical inputs, and the selected cycle count does not establish the physical time required to develop the same wear state in an actual high-speed transmission. The resulting worn geometry is used to update TVMS, LTE, and backlash. The dynamic speed is specified separately through W, while the effective wear coefficients and worn state are held fixed across the response maps. Thus, these calculations examine the dynamics of the

prescribed worn geometry rather than reconstructing the experimental operating history or predicting wear evolution at each scanned speed.

3.2.1. Wear Morphology and Meshing Characteristic Evolution

The final wear morphology is shown in Figure 9. Overall, the wear distribution exhibits a V-shaped pattern along the meshing/profile direction. The wear depth is larger near the two sides of the tooth surface, whereas it is relatively small near the pitch region. This is mainly because the relative sliding velocity is low near the pitch surface and gradually increases away from this region. Therefore, for each member under its prescribed loading-cycle count and the corresponding local load, greater material removal occurs on both sides of the tooth surface. For consistency, the horizontal coordinate in both panels of Figure 9 is defined on the common discretized contact grid. The pinion and face-gear wear values are evaluated at the same contact-point locations and are plotted using the same tooth-width coordinate and profile coordinate. Therefore, the horizontal axis represents the mapped tooth-width coordinate used for cross-surface comparison, rather than an independently defined native coordinate system for each gear surface.

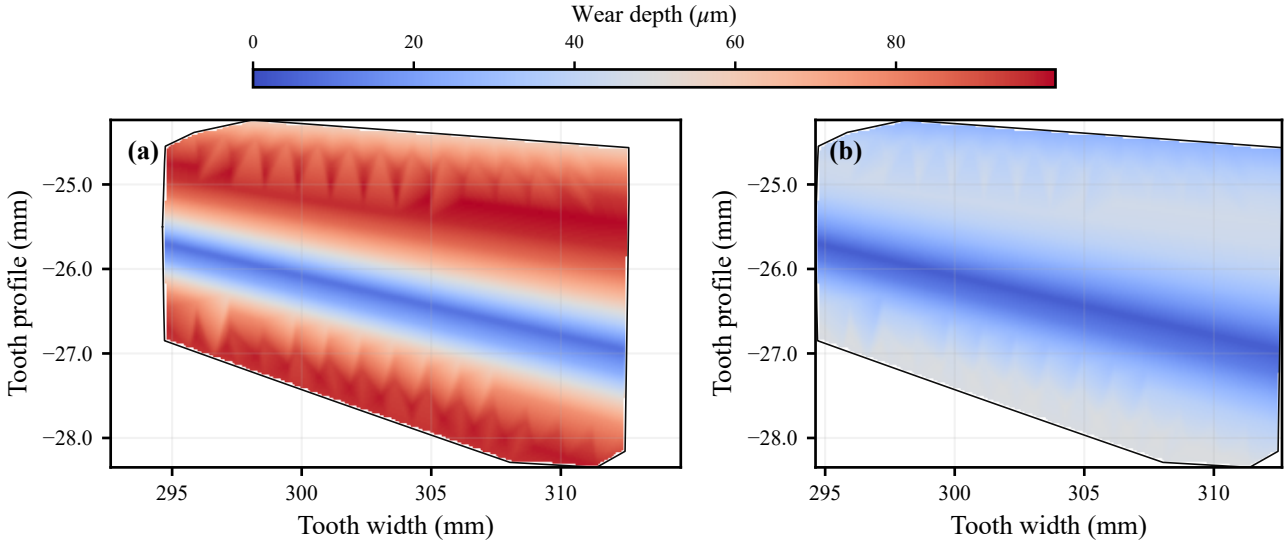


Figure 9. Final wear morphology of the face gear pair: (**a**) accumulated wear depth of the pinion; (**b**) accumulated wear depth of the face gear. Both panels use the same mapped tooth-width and profile coordinates on the common discretized contact grid to facilitate direct comparison of the two wear distributions. The same color scale is used for both surfaces to allow direct comparison of the wear severity.

As wear accumulates, the tooth-surface geometry changes and further affects the contact state and meshing characteristics of the gear pair. Figure 10 shows the evolution of TVMS, LTE, and clearance increase after wear. The phase-averaged TVMS is 196.601 MN/m for the unworn state and 196.423 MN/m for the worn state, corresponding to a reduction of 0.0905%. At individual meshing positions, the relative change reaches approximately 1.32%, indicating that wear still modifies the local mesh stiffness, although its effect on the phase-averaged value is small. In the present LTCA implementation, wear updates the local clearance and thus the active contact set and load distribution, while the global compliance matrix and curvature-derived local radii are retained. The local clearance is also subtracted from the loaded approach when calculating the elastic displacement used in the TVMS extraction. The small phase-averaged difference in Figure 10a is therefore specific to this implementation and should not be interpreted as evidence that wear has a generally

negligible effect on mesh stiffness. In contrast, the LTE fluctuation increases after wear, indicating that material removal modifies the loaded approach over the meshing phase.

Figure 10 also shows one-half of the wear-induced total clearance-width increase, $H/2$. The minimum scalar value is approximately 6.0 µm, whereas the full-field arithmetic mean in Equation (16) is 52.2 µm. The ten phase-dependent nodes range from 6.0 to 73.0 µm, with an arithmetic node mean of 47.2 µm. The phase average obtained by integrating the PCHIP-interpolated phase function over one mesh cycle is 47.1 µm. The full-field mean and the phase average use different spatial weights: the former averages all stored wear-grid entries, whereas the latter averages the phase-dependent interpolation over one mesh period. These plotted half-width quantities describe the increase in total clearance and are not the two contact thresholds used by the asymmetric dynamic model.

The unworn reference uses nominal tooth geometry without manufacturing or assembly errors. Its nearly flat mean-removed LTE fluctuation therefore represents an idealized reference rather than the transmission error of a manufactured gear pair.

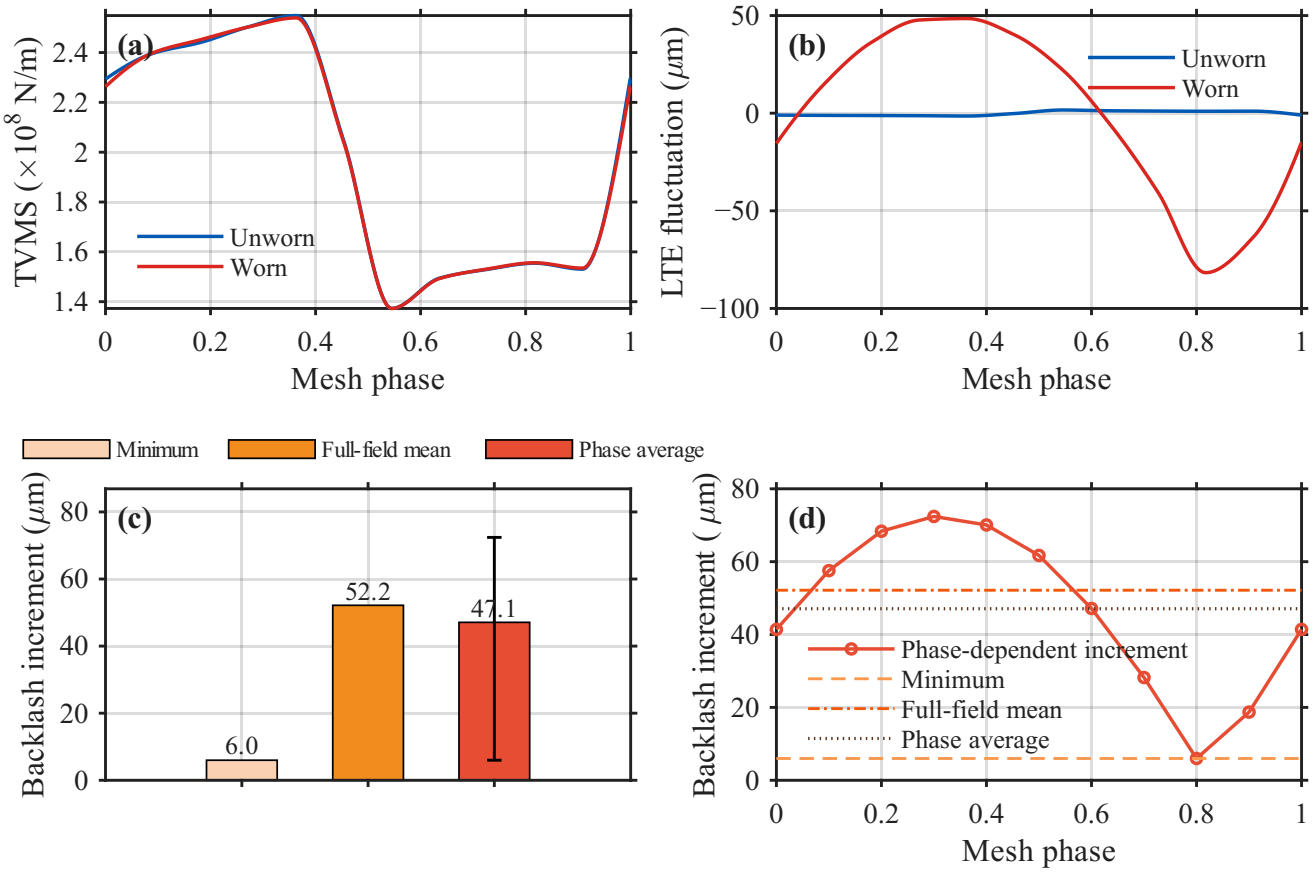


Figure 10. Evolution of meshing characteristics induced by wear: (**a**) TVMS of the unworn and worn tooth surfaces; (**b**) LTE fluctuation of the unworn and worn tooth surfaces; (**c**) minimum scalar, full-field mean, and phase average of the plotted half-clearance-width increment $H/2$; (**d**) phase-dependent $H(\phi)/2$ over one mesh cycle, with the minimum, full-field mean, and phase-average references. The full-field mean averages all stored wear-grid entries, whereas the phase average is obtained from the interpolated phase function over one mesh cycle. These half-width quantities visualize the total clearance increase; the asymmetric dynamic contact thresholds are defined separately in Equations (14) and (17). In (**c**), the whiskers show the minimum–maximum range of the phase nodes, rather than measurement uncertainty.

3.2.2. Nonlinear Response Maps Under the Worn Condition

The numerical response was evaluated over the dimensionless meshing frequency W and the initial half-backlash b_0. Figure 11 shows the resulting Poincaré displacement span.

The global scan uses W = 0.30:0.025:2.00 and b_0 = 0:2.5:90 μm, yielding 2553 parameter points and a pinion-speed range of approximately 4208–28,053 rpm. The scan covers the region around W = 1, where the sampled response changes markedly. The larger-span bands shift toward lower W as b_0 increases, and additional high-span regions appear around W = 1.0–1.35 for larger clearances.

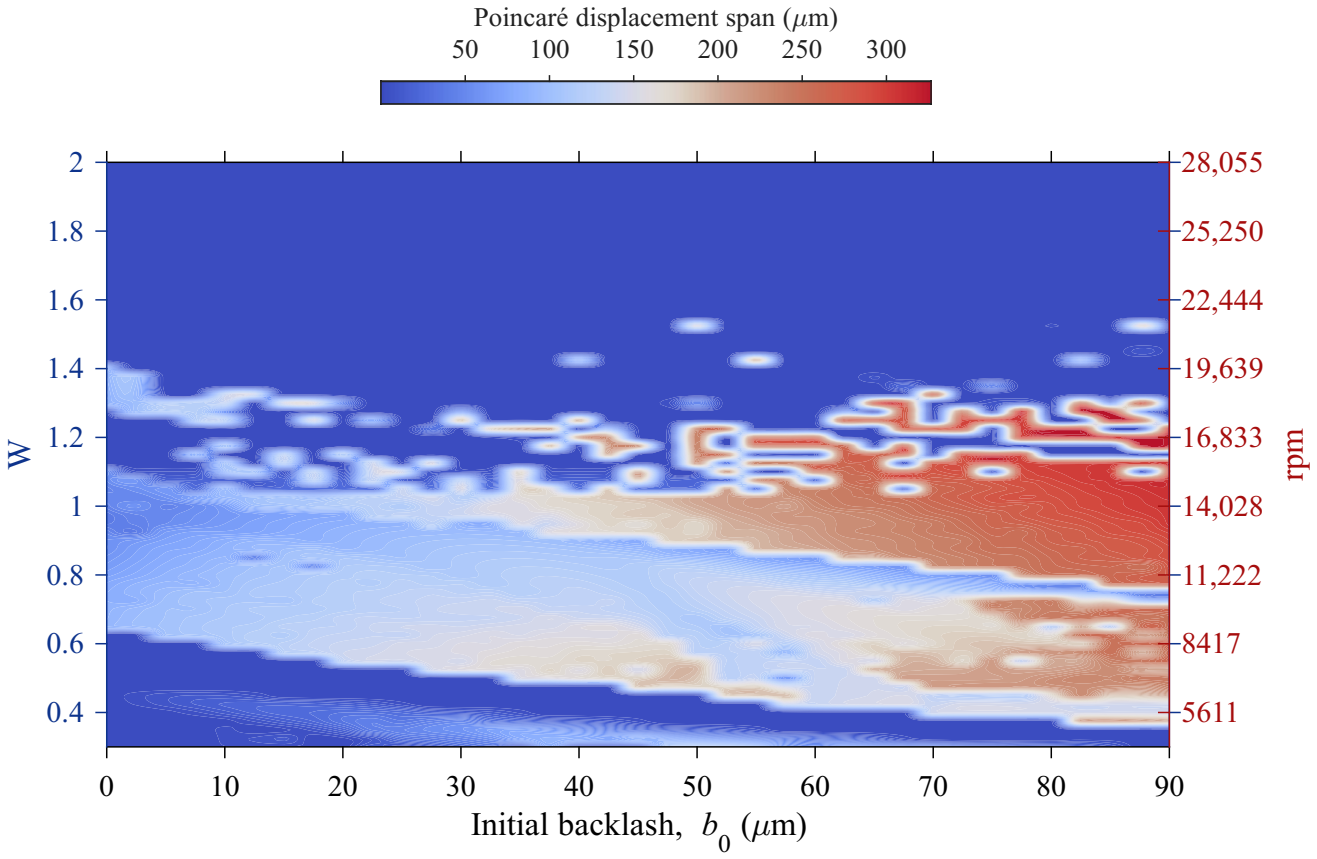


Figure 11. Global W–b_0 response screening map at 22 N·m, using steps of 0.025 in W and 2.5 μm in b_0 (2553 parameter points). The color denotes the Poincaré displacement span from a 150-mesh-period calculation. The right vertical axis indicates the equivalent pinion input speed in rpm.

Figure 12 shows a refined scan over W = 0.90–1.35 and b_0 = 50–110 μm, with increments of 0.01 and 2.5 μm, respectively. The scan contains 1150 points; each point is calculated for 150 mesh periods, and the displacement span is obtained from 76 retained samples. The maximum finite-window span is 377.82 μm at W = 1.19 and b_0 = 107.5 μm. Two cases at W = 1.19, P1 with b_0 = 92.5 μm and P2 with b_0 = 70 μm, are selected for the longer integrations below.

The corresponding parameter-sweep bifurcation diagrams in Figure 13 retain both displacement and velocity samples on the b_0 = 92.5 μm and W = 1.19 sections. The W section uses an increment of 0.01, and the b_0 section uses an increment of 1.25 μm. Each parameter point is initialized independently. These finite-window diagrams show response changes on the prescribed grids; the longer integrations of selected cases below are used to assess their late-time periodicity.

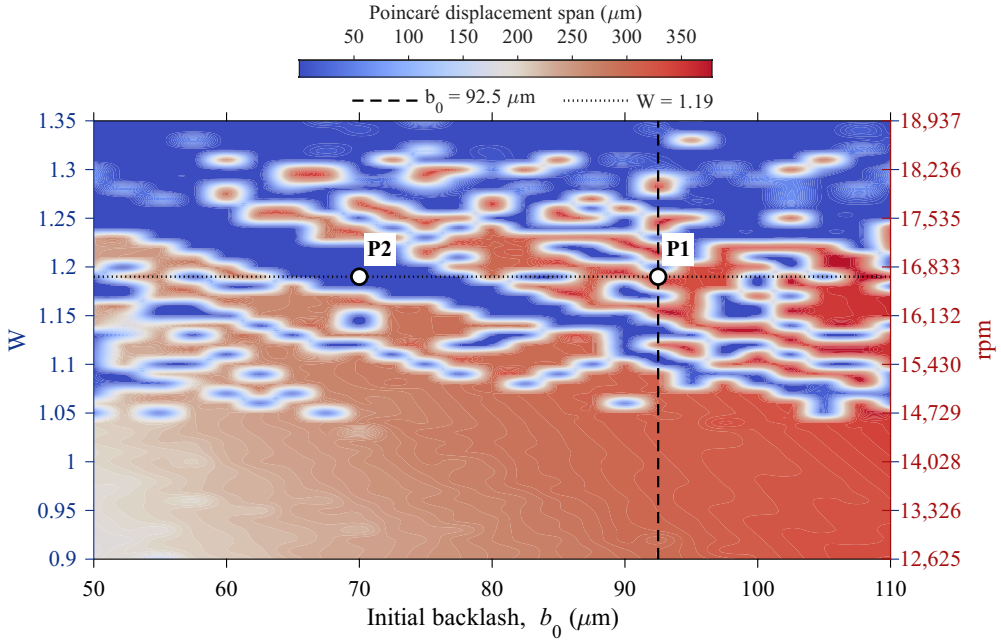


Figure 12. Refined W–b_0 response map under the worn condition at an input torque of 22 N·m, covering W = 0.90–1.35 and b_0 = 50–110 μm. The color denotes the Poincaré displacement span from 76 retained samples of each 150-mesh-cycle calculation. The dashed vertical and dotted horizontal lines mark b_0 = 92.5 μm and W = 1.19, respectively. P1 and P2 are marked at W = 1.19 and b_0 = 92.5 and 70 μm, respectively. Modified Akima interpolation is used only for displaying the color field. The right vertical axis indicates the equivalent pinion input speed in rpm.

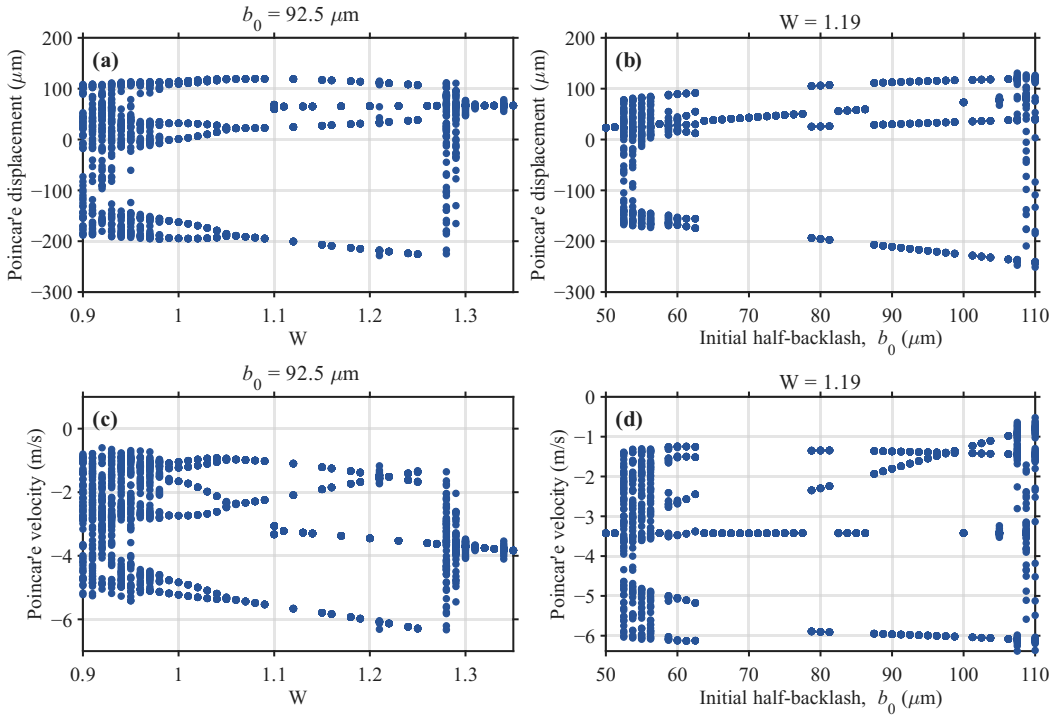


Figure 13. Parameter-sweep bifurcation diagrams under the worn condition at an input torque of 22 N·m: (**a**,**c**) Poincaré displacement and physical relative mesh-normal velocity versus W at b_0 = 92.5 μm; (**b**,**d**) Poincaré displacement and physical relative mesh-normal velocity versus b_0 at W = 1.19. The W section covers W = 0.90–1.35 with an increment of 0.01, and the b_0 section covers b_0 = 50–110 μm with an increment of 1.25 μm. The velocity is $v_n = b_c\omega_n\dot{\Delta}_n$ and is expressed in m/s. Each parameter point is calculated independently for 150 mesh cycles, and 76 paired samples at a fixed mesh phase are plotted.

3.2.3. Representative Dynamic Responses

Figure 14 shows P1 ($W = 1.19$, $b_0 = 92.5$ μm) and P2 ($W = 1.19$, $b_0 = 70$ μm) after 2000 mesh periods. Both use the worn TVMS and LTE, the asymmetric contact boundaries, and the default initial-condition pair $(a_0, v_0) = (0.05, 0.01)$. The corresponding pinion speed is approximately 16,693 rpm.

P1 forms three recurring Poincaré clusters with a displacement span of 328.59 μm. Its paired samples satisfy the period-3 repetition criterion in each 200-period window from cycles 200–400 onward, and its spectrum has a dominant component near one-third of the mesh frequency. The same period-3 response is obtained from all four tested initial-condition pairs. P2 forms a single cluster, with a final 80-sample span below 10^{-4} μm and a dominant component at the mesh frequency, consistent with a period-1 response.

The 0–1 diagnostic for P1 gives $K \approx -0.0067$ for all four initial conditions using the final 1600 samples, and $K \approx -0.0093$ using the final 1000. These values are close to zero and support the periodic interpretation together with the period-3 repetition test; the small negative correlations are finite-sample values.

P2 reaches this period-1 response from both the default and zero initial-condition pairs. The two larger initial perturbations produce higher-amplitude responses that persist to 2000 periods. Their Poincaré spans still decrease slightly between late sampling windows, so a settled period is not assigned to those responses. The P2 results shown here therefore describe the response reached from the stated default initial condition. The phase-sensitivity check gives the same period and cluster count at all five tested phases: P1 remains period 3 for all four initial-condition pairs, while P2 remains period 1 for the default and zero initial-condition pairs. The two larger-perturbation P2 responses do not satisfy the repetition criterion in the late 200-period windows at any tested phase and remain unclassified. The sampled coordinates and displacement span vary with phase; therefore, phase invariance is asserted only for the period and cluster count of the classified periodic responses, not for their point coordinates, span, or unclassified responses.

Figure 15 compares the dynamic mesh forces over the final ten mesh cycles of the same trajectories used in Figure 14. Both cases use an input torque of 22 N·m, corresponding to a nominal normal load of 925.4 N. The displacement fluctuation, dynamic load, and contact-state statistics in Table 3 are calculated over the final 80 mesh cycles. The displacement fluctuation RMS is $\sigma_x = [N_s^{-1} \sum_{i=1}^{N_s} (x_i - \bar{x})^2]^{1/2}$, and the dynamic amplification factor is $\max |F_\delta|$ divided by the nominal normal load. The contact-loss and back-side contact fractions correspond to $f_b = 0$ and $f_b < 0$, respectively.

For the stated initial condition, P1 has larger displacement fluctuation RMS, peak absolute mesh force, and back-side contact fraction than P2, while P2 has a larger contact-loss fraction. These numerical values refer to the two selected worn-system responses and do not describe all responses accessible from other initial conditions.

Table 3. Displacement fluctuation, dynamic load, and contact-state statistics over the final 80 mesh cycles of the 2000-cycle representative calculations at $W = 1.19$ and an input torque of 22 N·m, using the default initial-condition pair.

Metric	P1 ($b_0 = 92.5$ μm)	P2 ($b_0 = 70$ μm)
Displacement fluctuation RMS, σ_x (μm)	151.99	47.60
Maximum absolute dynamic mesh force (kN)	14.80	7.46
Dynamic amplification factor	16.00	8.06
Contact-loss fraction (%)	39.6	78.3
Back-side contact fraction (%)	21.6	0.0

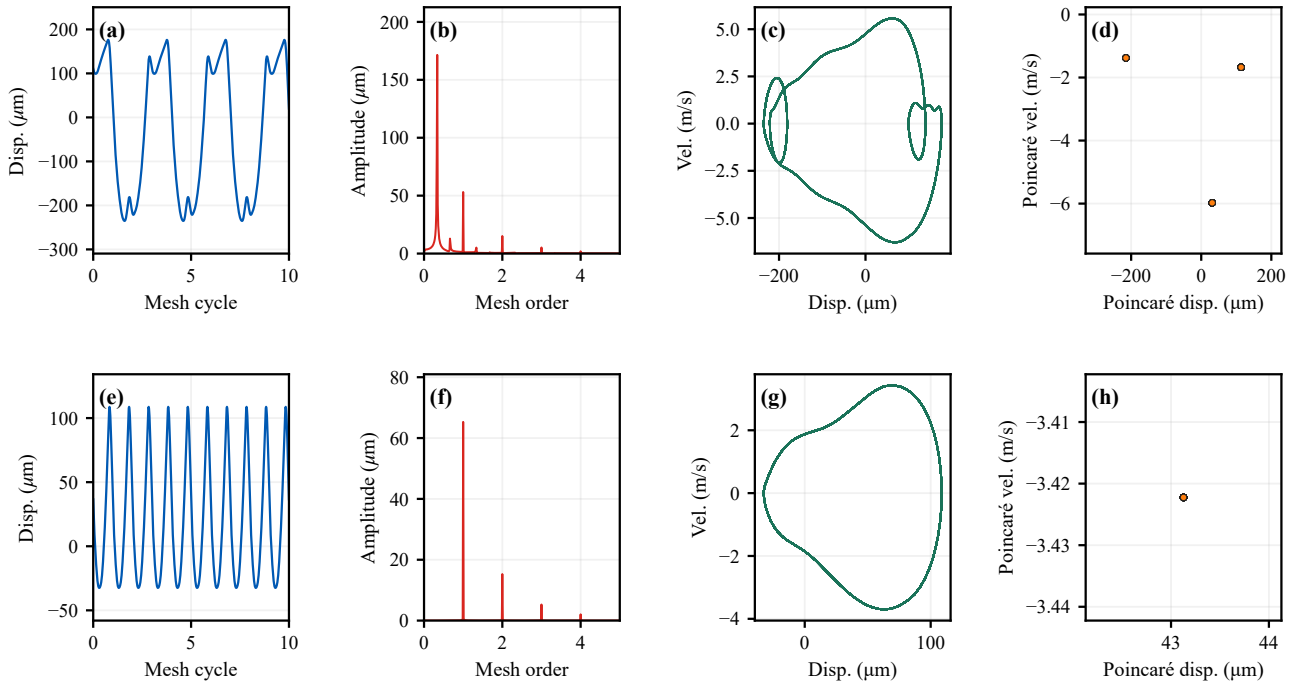


Figure 14. Representative dynamic responses at an input torque of 22 N·m and $W = 1.19$: (**a**) final ten-cycle displacement response at P1 ($b_0 = 92.5$ μm); (**b**) mesh-order spectrum at P1; (**c**) phase portrait at P1; (**d**) Poincaré section at P1; (**e**) final ten-cycle displacement response at P2 ($b_0 = 70$ μm); (**f**) mesh-order spectrum at P2; (**g**) phase portrait at P2; (**h**) Poincaré section at P2. Each case is integrated for 2000 mesh periods from the default initial-condition pair. The spectra use the final 80 cycles, and the Poincaré sections contain the final 80 paired samples. The phase portraits and Poincaré sections use displacement and physical relative mesh-normal velocity, $v_n = b_c \omega_n \dot{\Delta}_n$, in m/s. P1 exhibits a period-3 response, while P2 exhibits a period-1 response from this initial condition.

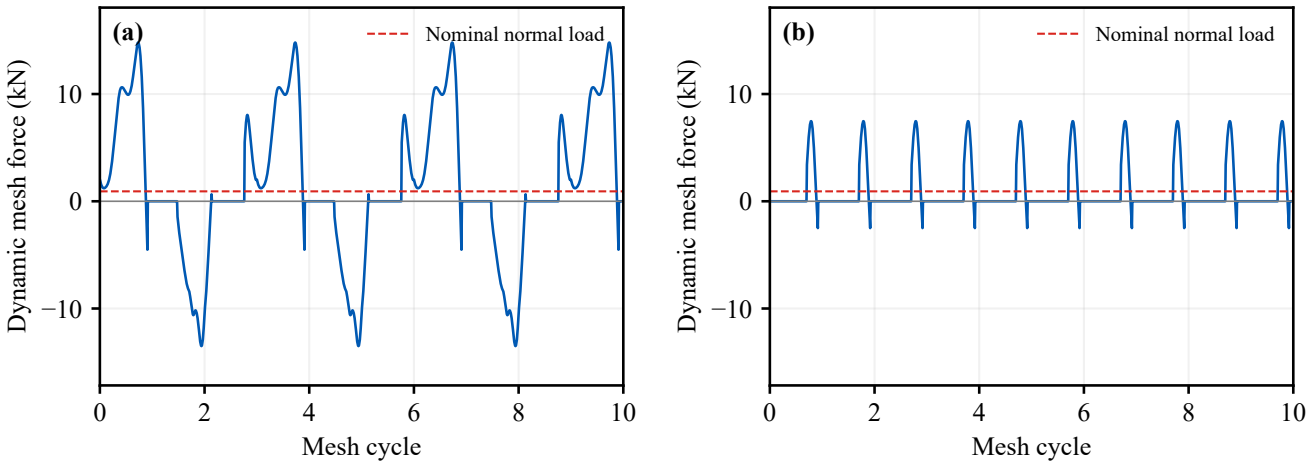


Figure 15. Dynamic mesh force over the final ten mesh cycles of the 2000-cycle worn-system calculations at an input torque of 22 N·m and $W = 1.19$: (**a**) P1 ($b_0 = 92.5$ μm); (**b**) P2 ($b_0 = 70$ μm). Both cases use the default initial-condition pair. The dashed line denotes the nominal normal load. The mesh-cycle origin is shifted to the start of the displayed window, and both panels use the same force scale.

3.2.4. Contribution Analysis and Backlash-Model Comparison

The control comparisons use $b_0 = 92.5$ and 70 μm, corresponding to P1 and P2, respectively. The four cases in Table 4 differ in whether worn TVMS/LTE and the wear-induced clearance increase are included. All cases use an input torque of 22 N·m, a

common physical input speed of 16,692.95 rpm, 2000 mesh periods, and the four initial-condition pairs specified in Section 2.3.5. Cases A and B use the unworn TVMS, for which $k_{\mathrm{mean,u}} = 1.96633 \times 10^8$ N/m and $\omega_{n,u} = 3.38019 \times 10^4$ rad/s; their actual dimensionless frequency is $W = 1.18945$. Cases C and D use the worn TVMS, for which $k_{\mathrm{mean,w}} = 1.96453 \times 10^8$ N/m and $\omega_{n,w} = 3.37864 \times 10^4$ rad/s; their actual value is $W = 1.19$. Thus, W is calculated using the natural-frequency reference for the TVMS state in each case, while the physical speed and physical initial velocity are held fixed.

The contact boundaries are constructed in the reference coordinate associated with each case's LTE. A and B use the unworn LTE and $\Delta e_{\mathrm{LTE}} = 0$; C and D use the worn LTE and $\Delta e_{\mathrm{LTE}} = e_w - e_u$. The recession input is $H = 0$ in A and C, and $H = H(\phi)$ in B and D. Substituting these quantities into $\delta_+ = b_0 + H - \Delta e_{\mathrm{LTE}}$ and $\delta_- = -b_0 - \Delta e_{\mathrm{LTE}}$ keeps the back-side boundary fixed in the nominal reference for every case.

Table 4. Definition of the control cases for contribution analysis.

Case	Worn TVMS/LTE	Wear-Induced Backlash	Meaning
A	×	×	Baseline
B	×	✓	Backlash only
C	✓	×	TVMS/LTE only
D	✓	✓	Coupled effect

Figure 16 compares the displacement fluctuation RMS and maximum absolute dynamic mesh force over the final 80 cycles. The bars show the default initial condition; the whiskers and open circles show the range and the other tested initial conditions, respectively. For P1, the default-initial-condition RMS values for A–D are 3.57, 4.02, 39.03, and 151.99 μm, with peak forces of 2.31, 6.80, 3.23, and 14.80 kN. For P2, the corresponding RMS values are 3.57, 127.16, 39.03, and 47.60 μm, and the peak forces are 2.31, 16.70, 3.23, and 7.46 kN. Thus, D gives the largest default-initial-condition values at P1, whereas B gives the largest values at P2.

A reaches a period-1 response and C a period-2 response from all four tested initial conditions at both clearances. B admits period-1 and period-3 responses depending on the initial condition. At P1, its RMS ranges from 4.02 to 148.90 μm and its peak force from 6.80 to 15.89 kN. At P2, the corresponding ranges are 4.02–127.16 μm and 6.80–16.70 kN. D retains the period-3 response at P1, while its P2 response depends on the initial condition as described above. The coupled update therefore does not give the largest response for every metric, clearance, and initial condition.

Figure 17 compares the Minimum, Full-field mean, Phase average, and Phase-dependent descriptions at 22 N·m and 16,692.95 rpm ($W = 1.19$ for the worn system), using b_0 = 50:2.5:110 μm. All four retain the same worn TVMS/LTE, asymmetric contact law, and LTE coordinate shift. The three scalar half-width increments are 5.9819, 52.1655, and 47.0843 μm, respectively. Each model is evaluated at all 25 clearances from each of the four initial-condition pairs in Section 2.3.5, giving 400 independent 2000-period trajectories. The Poincaré span uses the final 80 paired samples; the displacement fluctuation RMS and peak force use the final 80 periods. Solid curves show the default initial condition, dashed curves the other three, and shading the range across the four tested initial conditions.

Across the tested clearances and initial conditions, the phase-dependent description gives a displacement fluctuation RMS of 47.60–166.50 μm and a peak absolute mesh force of 7.46–20.42 kN. The corresponding ranges across the three scalar descriptions are 39.03–44.11 μm and 3.23–5.74 kN. At every clearance, even the lowest phase-dependent RMS and peak force across the four initial conditions exceed the highest corresponding Phase average values. The smallest separations are 3.48 μm and 1.72 kN, respectively. Thus, this

ordering persists over the four tested initial conditions after matching the mean clearance width. It refers to the stated observation window and does not establish a ranking over untested initial states or operating conditions.

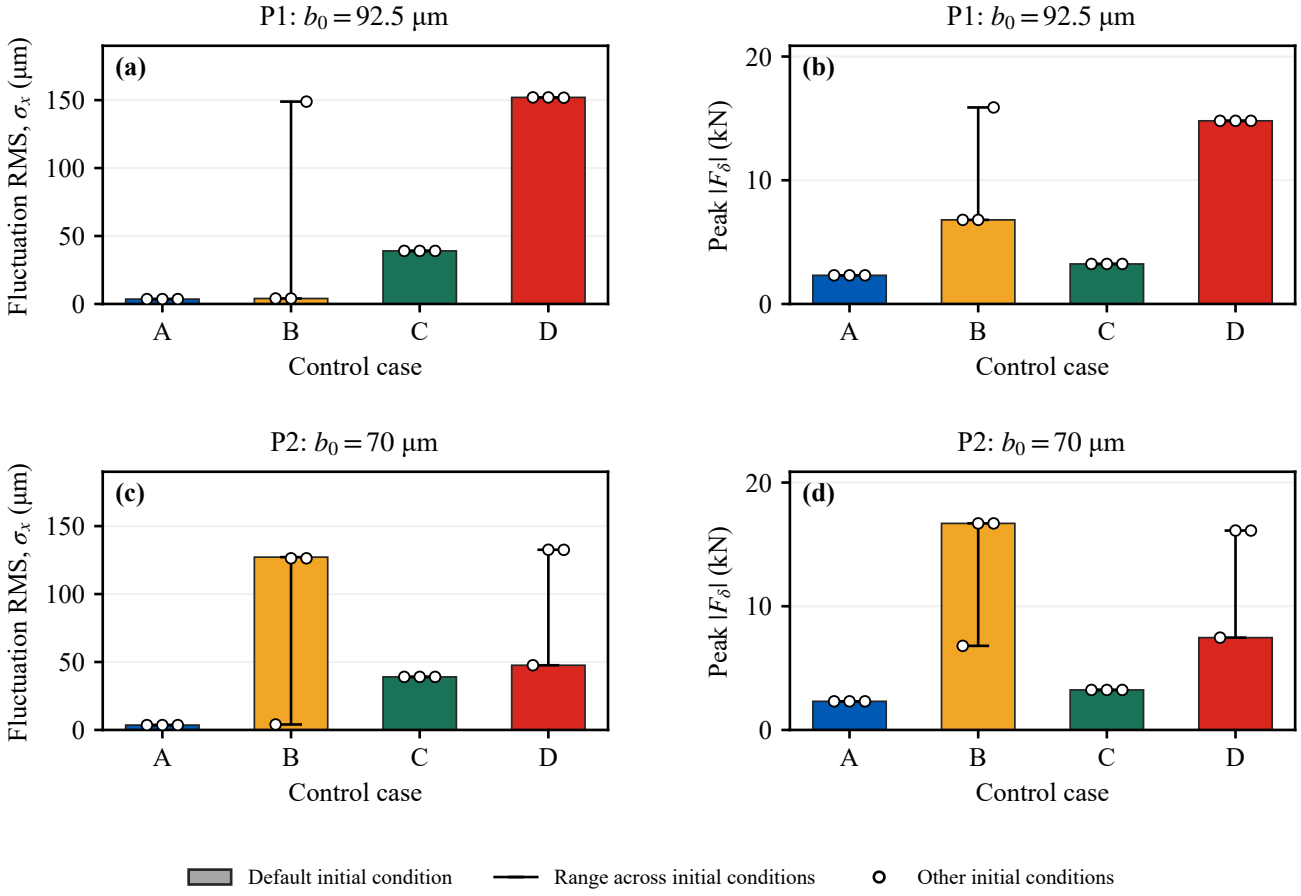


Figure 16. Contribution analysis at 22 N·m and a common physical speed of 16,692.95 rpm ($W = 1.19$ for the worn system): (**a**,**b**) displacement fluctuation RMS and maximum absolute mesh force at P1, $b_0 = 92.5$ μm; (**c**,**d**) the same metrics at P2, $b_0 = 70$ μm. A–D denote the baseline, backlash-only, worn-TVMS/LTE-only, and coupled cases. Bars show the default initial condition, whiskers span all four tested initial conditions, and open circles show the other three. The ranges describe initial-condition dependence, not measurement uncertainty. All metrics use the final 80 periods of 2000-period calculations.

The Poincaré span ranges from approximately zero to 361.05 μm for the phase-dependent model and from 0.10 to 40.87 μm for the scalar descriptions. Its ordering is less robust: the phase-dependent span is larger than the matched-mean span for all four initial conditions at eight clearances and smaller at two; at the other fifteen, the ordering changes with the initial condition. For example, at $b_0 = 70$ μm, the phase-dependent response is period 1 from the default and zero initial conditions, while the larger initial perturbations retain a high-response branch. The scalar descriptions also reach different periodic branches at some clearances. A small span therefore does not imply a small RMS or peak force.

The last two 200-period windows identify the same period candidate for 391 of the 400 trajectories. The remaining nine are phase-dependent responses: all four initial conditions at $b_0 = 55$ μm, the two larger perturbations at 57.5 and 70 μm, and the fourth initial condition at 60 μm. The last of these gives a period-24 candidate only in the final window, while the others fail the repetition criterion there. These responses remain unclassified; their final-window metrics are retained in the comparison without treating them as converged attractors.

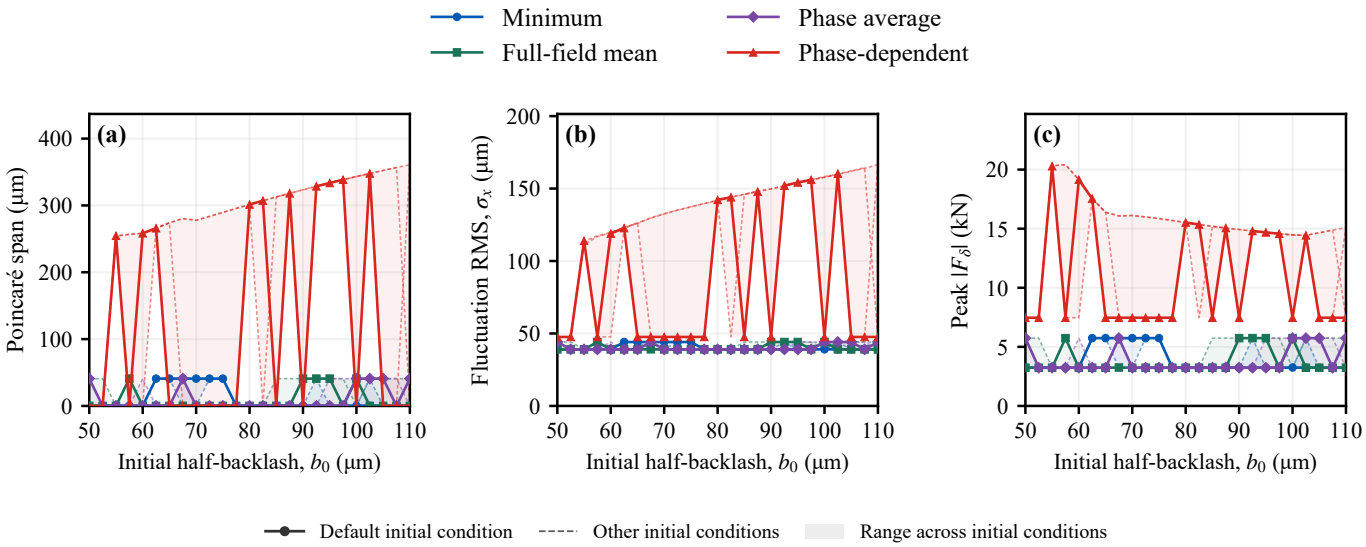


Figure 17. Comparison of four clearance-width descriptions with identical worn TVMS/LTE and asymmetric contact boundaries at 22 N·m and 16,692.95 rpm ($W = 1.19$), using b_0 = 50:2.5:110 μm: (**a**) Poincaré displacement span; (**b**) displacement fluctuation RMS; (**c**) maximum absolute dynamic mesh force. Full-field mean averages the stored wear grid; Phase average integrates the actual periodic interpolation. Each model–clearance combination is integrated independently for 2000 mesh periods from each of four initial conditions. Solid curves show the default initial condition, dashed curves the other three, and shading the minimum–maximum range across them. Panel (**a**) uses the final 80 paired samples; panels (**b**,**c**) use the final 80 periods. Lines join computed points without smoothing; shading represents initial-condition dependence rather than measurement uncertainty.

3.2.5. Damping Sensitivity at P1 and P2

For P1, the final-window period-3 candidate persists for $\zeta = 0.04$–0.10 (Figure 18). Over these points, displacement RMS decreases from 153.96 to 151.04 μm and peak force from 15.15 to 14.67 kN. At $\zeta = 0.12$, a period-1 candidate is identified, with RMS, and peak force of 47.42 μm and 8.27 kN. Contact loss increases from 38.6–39.9% to 78.3%, while back-side contact decreases from 21.3–22.4% to zero (Table 5). This change between $\zeta = 0.10$ and 0.12 indicates a different response state for this initial-condition branch, rather than a smooth monotonic dependence on damping. For P2, all five damping values satisfy the period-1 repetition criterion in the final two 200-period windows. As ζ increases from 0.04 to 0.12, displacement RMS decreases from 47.80 to 47.42 μm (0.80%), whereas peak absolute mesh force increases from 6.86 to 8.27 kN (20.44%). The total mesh force includes both elastic and viscous terms, so a reduction in displacement fluctuation need not coincide with a lower peak force. Contact loss remains 77.5–78.3%, and no back-side contact occurs. The two representative cases therefore respond differently to the damping variation under the prescribed default initial condition.

Table 5. Damping-sensitivity metrics for P1 and P2. Response statistics use the final 80 mesh periods of each 2000-period calculation; period candidates use the final 200-period window.

Case	ζ	Period Candidate	σ_x (μm)	Peak $\|F_\delta\|$ (kN)	Contact Loss (%)	Back-Side Contact (%)
P1	0.04	3	153.96	15.15	38.6	22.4
P1	0.06	3	152.88	14.96	39.1	21.8
P1	0.08	3	151.99	14.80	39.6	21.6
P1	0.10	3	151.04	14.67	39.9	21.3
P1	0.12	1	47.42	8.27	78.3	0.0

Table 5. *Cont.*

Case	ζ	Period Candidate	σ_x (μm)	Peak $\lvert F_\delta \rvert$ (kN)	Contact Loss (%)	Back-Side Contact (%)
P2	0.04	1	47.80	6.86	77.5	0.0
P2	0.06	1	47.70	7.14	77.5	0.0
P2	0.08	1	47.60	7.46	78.3	0.0
P2	0.10	1	47.50	7.85	78.3	0.0
P2	0.12	1	47.42	8.27	78.3	0.0

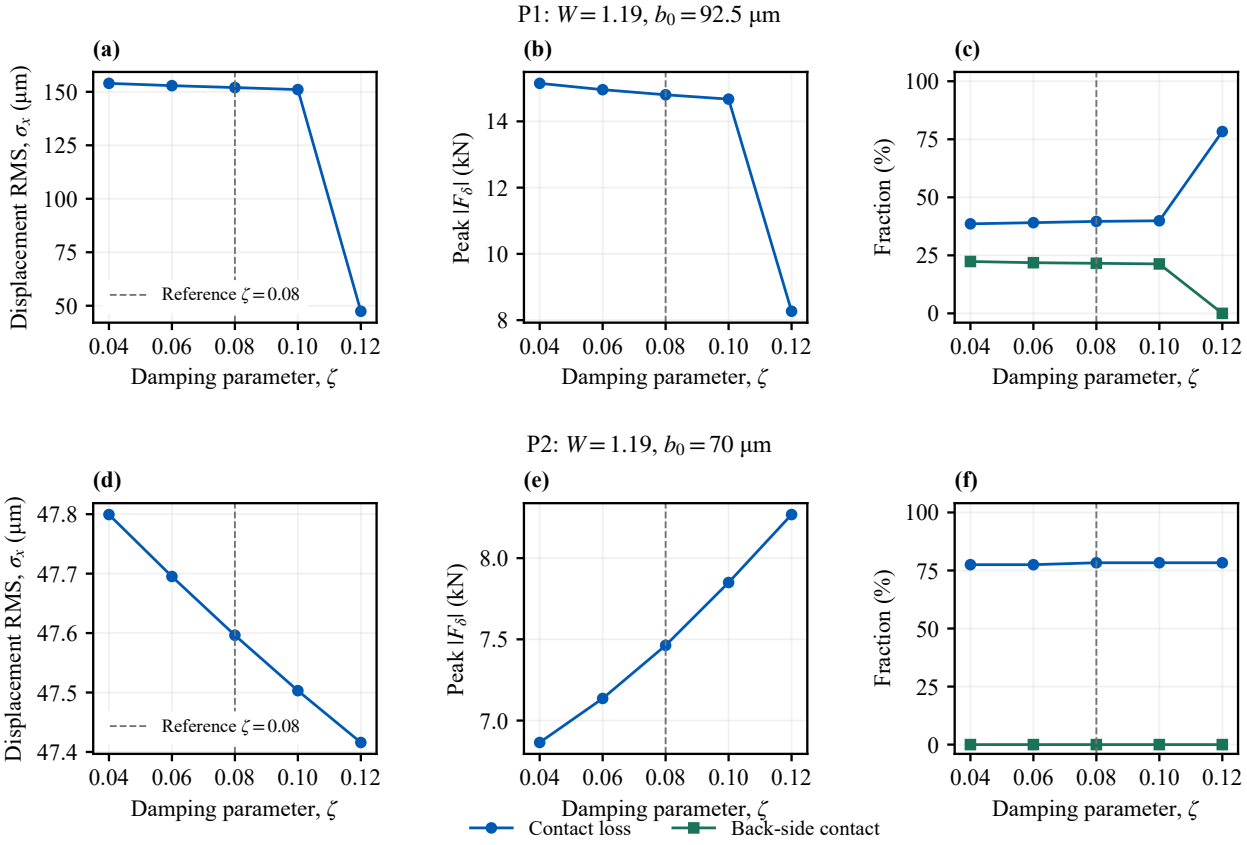


Figure 18. Damping sensitivity of P1 and P2 at 22 N·m, W = 1.19, and 16,692.95 rpm: (**a**–**c**) P1, b_0 = 92.5 μm; (**d**–**f**) P2, b_0 = 70 μm. The columns show displacement fluctuation RMS, peak absolute dynamic mesh force, and contact-loss/back-side contact fractions, respectively. Each point uses a separate 2000-period calculation with the same default initial condition, worn TVMS/LTE, and asymmetric contact law; statistics use the final 80 periods. Dashed lines mark ζ = 0.08. The solid lines connect the five tested values without locating a critical damping parameter.

3.2.6. Backlash-Model Comparison with Moderate Contact Loss

An additional comparison is made at W = 0.15, b_0 = 70 μm, and ζ = 0.08, corresponding to 2104.15 rpm and 22 N·m. The phase-dependent model gives approximately 15% contact loss, providing a less intermittent condition than P1 and P2. The same prescribed worn geometry, TVMS, LTE, asymmetric contact law, and default initial condition are used for all four models; wear is not re-evolved at the lower dynamic speed. The Phase average increment remains matched to the cycle integral of the phase-dependent input.

As shown in Figure 19, the three scalar models agree to the reported precision, giving a displacement fluctuation RMS of 44.81 μm, peak absolute mesh force of 3.143 kN, and contact loss of 12.50%. The phase-dependent model gives 4.19 μm, 2.960 kN, and 15.00%, respectively. Relative to Phase average, the RMS and peak force decrease by 90.65% and 5.82%, while contact

loss increases by 2.50 percentage points. None of the four responses has back-side contact, and all satisfy the period-1 repetition criterion in the final two 200-period windows.

The three scalar trajectories differ mainly by a constant shift in mean relative displacement. With no back-side contact in these late responses, this shift leaves the displacement fluctuation and mesh force almost unchanged. The phase-dependent input instead changes the boundary over each cycle. Its lower RMS and peak force here, compared with the opposite ordering at $W = 1.19$, show that the effect of phase modulation depends on the operating condition even when the mean clearance width is matched.

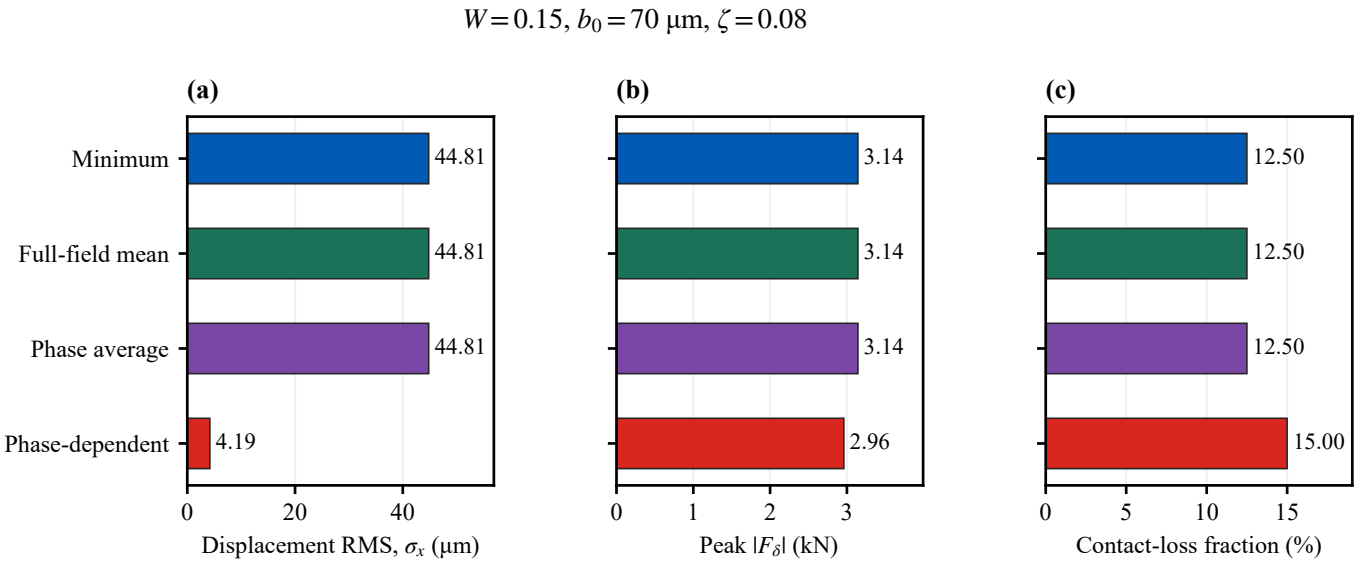


Figure 19. Four-model comparison at $W = 0.15$, $b_0 = 70$ μm, $\zeta = 0.08$, 22 N·m, and 2104.15 rpm: (**a**) displacement fluctuation RMS; (**b**) peak absolute dynamic mesh force; (**c**) contact-loss fraction. All models use identical worn TVMS/LTE, asymmetric contact expressions, physical speed, default initial condition, and integration settings. The constant half-width increments are 5.9819, 52.1655, and 47.0843 μm for Minimum, Full-field mean, and Phase average, respectively; the last matches the cycle average of Phase-dependent. Statistics use the final 80 periods of separate 2000-period calculations.

4. Discussion

The matched-mean comparisons distinguish clearance-width modulation from the mean clearance level. At $W = 1.19$, the phase-dependent model gives larger displacement fluctuation RMS and peak mesh force than Phase average throughout the tested clearance range, with separated metric ranges across the four tested initial conditions. In contrast, the Poincaré-span ordering changes with the initial condition at fifteen clearances, and the locations of individual branch changes are not initial-state independent. At the supplementary $W = 0.15$, $b_0 = 70$ μm condition, the phase-dependent model gives lower RMS and peak force from the default initial condition despite the same mean clearance width. Phase modulation therefore affects the response without imposing a universal ordering. The Poincaré span measures the spread of fixed-phase samples, rather than the amplitude of the continuous response, and should be interpreted alongside RMS and dynamic load.

At a fixed W, changing the initial half-backlash b_0 alters the paired displacement–velocity Poincaré structure, displacement fluctuation, and dynamic mesh force. The response therefore does not change monotonically with clearance over the examined range.

The 3.48% maximum-wear difference concerns only the reported maxima after calibration; it does not characterize the accuracy of the whole wear profile. The tooth-surface measurements were used both to identify the effective wear coefficient and to construct the comparison profile. The available measurement documentation does not support an

uncertainty estimate or a tooth-to-tooth statistical assessment. A separate, traceable dataset would be required for independent validation.

The contribution analysis shows that the coupled wear update need not give a larger response than either isolated update. At P2, the backlash-only case gives larger default-initial-condition RMS and peak force than the coupled case. Several comparisons also depend on the initial condition. The effect of an excitation update therefore cannot be inferred from its magnitude alone; the response branch reached under the stated conditions must also be considered.

The damping sweep retains a period-3 candidate at P1 for $\zeta = 0.04$–0.10 and a period-1 candidate at $\zeta = 0.12$, whereas P2 remains period 1 at all five values for the default initial condition. The P2 peak force increases while its displacement RMS decreases slightly. These results do not establish a critical damping parameter or a general monotonic damping trend, because only five discrete values and one initial-condition branch are examined.

The dynamic mesh force uses phase-dependent TVMS in a linear spring relation, with separation and flank switching represented by the piecewise contact law. The stiffness is not updated with the instantaneous dynamic load, and local tooth-impact compliance is not resolved. Repeated separation, re-contact, and high transient forces therefore limit the interpretation of the predicted peak loads. The supplementary moderate-contact-loss case shows a phase-modulation effect under less intermittent contact, but does not validate local impact loads. Load-dependent contact stiffness and local impact response require further modeling.

The model also uses condition-specific effective wear coefficients and a Hertzian peak-pressure approximation. The wear update changes the contact gap while retaining the nominal TCA path and local curvatures, and the periodic input assumes identical wear from tooth to tooth. All four clearance-width descriptions use the same asymmetric contact law; the scalar cases replace only the recession input H, retaining the worn LTE reference shift. The experimental comparison uses calibration data and presents the pinion profile, while the torque comparison checks only kinematic mesh-frequency consistency at the tested low speed and does not independently validate the dynamics. The measured torque is a system-level signal, and its additional spectral peaks are not used to identify separate gear-mesh components without order tracking or component-level measurements. The high-speed response amplitudes and loads remain numerical predictions. The model comparisons apply to the stated speed, clearances, initial conditions, and observation interval. Some high-response trajectories still vary over the late sampling windows, so a fixed 2000-period duration is not treated as proof of convergence. Material- and fluid-dependent wear evolution, impact damage, and a definitive chaos classification are outside the present model.

5. Conclusions

A coupled wear–dynamics framework was developed for a worn face gear pair. The worn tooth surface was used to update TVMS, LTE, and backlash before the dynamic calculation. The main conclusions are as follows.

(1) Wear is nonuniform along the meshing path, with lower wear near the pitch region and higher wear toward both sides of the contact region. In the examined case, LTE and backlash change more markedly with wear than TVMS, and the wear-induced backlash varies with mesh phase.

(2) The phase-dependent model retains the mesh-phase variation and represents single-sided working-flank wear using separate working-side and back-side thresholds in the LTE-referenced coordinate. Three scalar descriptions use the same asymmetric formulation while replacing the geometric recession input by its minimum, full-field mean, or phase integral mean. The phase integral mean provides a comparison at matched mean clearance width.

(3) The response maps and parameter-sweep bifurcation diagrams show a nonmonotonic dependence on dimensionless meshing frequency and initial half-backlash. At $W = 1.19$, the 2000-period calculations identify a period-3 response for P1 ($b_0 = 92.5$ μm) from all four tested initial conditions. P2 ($b_0 = 70$ μm) reaches a period-1 response from the default and zero initial conditions, while larger initial perturbations retain higher-amplitude responses over the computed interval. The Poincaré span is used for screening; period identification also uses paired displacement–velocity repetition and successive sampling windows.

(4) The four-initial-condition contribution analysis shows that backlash-only and coupled updates can reach different response branches. With the default initial condition, the coupled case gives the largest RMS and peak force at P1, whereas the backlash-only case gives the largest values at P2. The ordering is therefore conditional on the clearance, response metric, and initial condition.

(5) At $W = 1.19$ and $b_0 = 50{:}2.5{:}110$ μm, the phase-dependent model gives larger displacement fluctuation RMS and peak absolute mesh force than the scalar case with the same mean clearance width over all four tested initial conditions. At each clearance, the four-initial-condition ranges of these metrics remain separated in the final 80 periods of the 2000-period calculations. Their Poincaré-span ordering changes with the initial condition at fifteen of the 25 clearances, so span-based point counts do not describe an initial-state-independent distinction. At the supplementary $W = 0.15$, $b_0 = 70$ μm condition, the phase-dependent model instead gives lower RMS and peak force than the matched-mean scalar from the default initial condition. Phase modulation thus affects the response beyond the mean clearance level, with its influence depending on the examined operating condition and response branch.

The experimental work provides contact-trace assessment, wear-coefficient calibration, and a low-speed kinematic mesh-frequency consistency check. Figure 8 checks rotational-speed and mesh-frequency consistency rather than independently validating the dynamic model; the additional peaks in the torque record remain unidentified. The response maps and high-speed dynamic results are numerical outcomes for the prescribed worn state and should be interpreted together with the worn TVMS, LTE, and phase-dependent contact boundary. The severe-wear reference state was selected to have a maximum pinion wear depth comparable to the experimental value; it is not used to determine an allowable wear limit or the remaining service life of the transmission. The dynamic results also depend on the prescribed equivalent masses and inertias, which have not been validated against the actual mass distribution of the face gear. Accordingly, the conclusions are limited to the examined face-gear pair, prescribed mass properties and wear state, torque and speed ranges, clearance range, damping values, initial conditions, and observation windows. They do not establish absolute-amplitude validation, higher-speed experimental validity, or a universal response ordering for other systems or operating conditions.

Supplementary Materials: The following supporting information can be downloaded at https://www.mdpi.com/article/10.3390/app162110933/s1, Supplementary File S1 provides the numerical inputs for the dynamic calculations: unworn and worn TVMS/LTE samples, the Fourier coefficients used by the solver, wear-recession and LTE-reference nodes, separate contact thresholds, scalar clearance references, and the associated numerical parameters and case definitions. Units, phase conventions, and interpolation are documented in the accompanying README and data dictionary.

Author Contributions: Y.Y. led the conceptualization and methodology development, implemented the software, performed the validation, formal analysis, and investigation, curated the data, prepared the visualizations, and wrote the original draft. Y.S. contributed to the conceptualization, supervised the research, and reviewed and edited the manuscript. X.P. contributed to methodology development and validation, led the experimental investigation, provided experimental resources, coordinated the

project, and reviewed and edited the manuscript. P.F. assisted with formal analysis, data curation, and visualization. X.L. contributed to the gear dynamics and loaded tooth contact analysis methods, acquired funding, provided resources, and reviewed and edited the manuscript. All authors have read and agreed to the published version of the manuscript.

Funding: This research was funded by the National Natural Science Foundation of China (NSFC), grant number 52675189.

Institutional Review Board Statement: Not applicable.

Informed Consent Statement: Not applicable.

Data Availability Statement: The processed numerical inputs used in the dynamic calculations are supplied in Supplementary File S1. The underlying tooth-surface measurements and torque records, restricted material and heat-treatment information, surface roughness, and test-liquid identity are not publicly available because of project confidentiality requirements. These restrictions limit independent verification of the experimental calibration and comparisons. Computational source code is not provided.

Conflicts of Interest: The authors declare that they have no known competing financial interests or personal relationships that could have appeared to influence the work reported in this paper.

References

1. Litvin, F.L.; Fuentes, A. *Gear Geometry and Applied Theory*, 2nd ed.; Cambridge University Press: Cambridge, UK, 2004.
2. Litvin, F.L.; Fuentes, A.; Zanzi, C.; Pontiggia, M.; Handschuh, R.F. Face-gear drive with spur involute pinion: Geometry, generation by a worm, stress analysis. *Comput. Methods Appl. Mech. Eng.* **2002**, *191*, 2785–2813. [CrossRef]
3. Liu, L.; Zhu, L.; Gou, X. Modeling and analysis of load distribution ratio and meshing stiffness for orthogonal spur-face gear drive under point contact. *Mech. Mach. Theory* **2023**, *182*, 105239. [CrossRef]
4. Park, D.; Kolivand, M.; Kahraman, A. Prediction of surface wear of hypoid gears using a semi-analytical contact model. *Mech. Mach. Theory* **2012**, *52*, 180–194. [CrossRef]
5. Park, D.; Kolivand, M.; Kahraman, A. An approximate method to predict surface wear of hypoid gears using surface interpolation. *Mech. Mach. Theory* **2014**, *71*, 64–78. [CrossRef]
6. Zhou, C.; Wang, H. An adhesive wear prediction method for double helical gears based on enhanced coordinate transformation and generalized sliding distance model. *Mech. Mach. Theory* **2018**, *128*, 58–83. [CrossRef]
7. Wang, H.; Zhou, C.; Wang, H.; Hu, B.; Liu, Z. A novel contact model for rough surfaces using piecewise linear interpolation and its application in gear wear. *Wear* **2021**, *476*, 203685. [CrossRef]
8. Wang, H.; Tang, L.; Zhou, C.; Shi, Z. Wear life prediction method of crowned double helical gear drive in point contact mixed elastohydrodynamic lubrication. *Wear* **2021**, *484–485*, 204041. [CrossRef]
9. Tian, H.; Han, H.; Zhao, Z.; Han, C.; Ma, H. Wear prediction and meshing characteristics for the planetary gear set considering angular misalignment and rotating carrier. *Eng. Fail. Anal.* **2022**, *140*, 106583. [CrossRef]
10. Sun, Y.; Li, Y.; Zhang, Q.; Qin, X.; Chen, K. Wear analysis and simulation of small module gear based on Archard model. *Eng. Fail. Anal.* **2023**, *144*, 106990. [CrossRef]
11. Peng, X.; Yue, H.; Zhou, J. Dynamic response and typical characteristics analysis of tooth surface wear of face gear pair. *J. Vib. Shock* **2023**, *42*, 323–330. (In Chinese)
12. Pathak, M.; Jayanti, L.; Rakshit, S. Linear complementarity formulations for contact analysis and wear prediction in gears. *Mech. Mach. Theory* **2024**, *198*, 105669. [CrossRef]
13. Walker, J.; Mohammadpour, M.; Theodossiades, S.; Bewsher, S.; Offner, G.; Bansal, H.; Leighton, M.; Braunstingl, M.; Flesch, H.-G. A multi-physics transient wear model for helical gear pairs. *Tribol. Int.* **2022**, *169*, 107463. [CrossRef]
14. Guan, Y.; Chen, J.; Fang, Z.; Hu, S. A quick multi-step discretization and parallelization wear simulation model for crown gear coupling with misalignment angle. *Mech. Mach. Theory* **2022**, *168*, 104576. [CrossRef]
15. Wang, H.; Feng, S.; Yin, L.; Hu, B.; Su, J.; Liu, H.; Zhou, C. A calculation method of gear tooth surface wear considering the center distance error. *Wear* **2025**, *570*, 206006. [CrossRef]
16. Shen, Z.; Qiao, B.; Yang, L.; Luo, W.; Chen, X. Evaluating the influence of tooth surface wear on TVMS of planetary gear set. *Mech. Mach. Theory* **2019**, *136*, 206–223. [CrossRef]
17. Shen, Z.; Qiao, B.; Yang, L.; Luo, W.; Yang, Z.; Chen, X. Fault mechanism and dynamic modeling of planetary gear with gear wear. *Mech. Mach. Theory* **2021**, *155*, 104098. [CrossRef]

18. Shen, Z.; Yang, L.; Qiao, B.; Luo, W.; Chen, X.; Yan, R. Mesh relationship modeling and dynamic characteristic analysis of external spur gears with gear wear. *Front. Mech. Eng.* **2022**, *17*, 9. [CrossRef]
19. Chang, L.; Liu, G.; Wu, L. A robust model for determining the mesh stiffness of cylindrical gears. *Mech. Mach. Theory* **2015**, *87*, 93–114. [CrossRef]
20. Liu, N.; Ma, H.; Zhao, Z.; Wang, P.; Zhao, X. Dynamic characteristics of gear-rotor system with gear eccentricity and wear fault. *Nonlinear Dyn.* **2024**, *112*, 16003–16035. [CrossRef]
21. Liu, X.; Fang, Z.D.; Lei, F.J.; Kang, H.; Han, H.; Shen, Y.; Dong, H.; Fu, X. A novel method to study the long period three-dimensional vibration characteristics of herringbone gear with asymmetry pitch deviation. *Mech. Syst. Signal Process.* **2025**, *224*, 112040. [CrossRef]
22. Zhang, K.; Shen, R.; Hu, Z.; Tang, J.; Sun, Z.; Ning, A.; Yang, S. Dynamic modeling and analysis considering friction-wear coupling of gear system. *Int. J. Mech. Sci.* **2024**, *275*, 109343. [CrossRef]
23. Li, Z.; Xiao, H.; Tang, Y.; Liang, G.; Wang, L.; Yang, J. A deterministic model of surface profile degradation for evaluating time-varying mesh stiffness and dynamic responses of spur gear considering tooth surface wear evolution. *Mech. Syst. Signal Process.* **2025**, *225*, 112313. [CrossRef]
24. Li, Z.; Chen, Z.; Guo, L.; Zhai, W. Nonlinear dynamics of gear transmission with an improved wear model. *Int. J. Mech. Sci.* **2025**, *299*, 110399. [CrossRef]
25. Huangfu, Y.; Zhao, Z.; Ma, H.; Han, H.; Chen, K. Effects of tooth modifications on the dynamic characteristics of thin-rimmed gears under surface wear. *Mech. Mach. Theory* **2020**, *150*, 103870. [CrossRef]
26. Chen, W.; Lei, Y.; Fu, Y.; Hou, L. A study of effects of tooth surface wear on time-varying mesh stiffness of external spur gear considering wear evolution process. *Mech. Mach. Theory* **2021**, *155*, 104055. [CrossRef]
27. Sánchez, M.B.; Pleguezuelos, M.; Pedrero, J.I. Influence of profile modification on the transmission error of spur gears under surface wear. *Mech. Mach. Theory* **2024**, *191*, 105473. [CrossRef]
28. Chen, Z.; Ji, P. Research on the variation of mesh stiffness and transmission error for spur gear with tooth profile modification and wear fault. *Eng. Fail. Anal.* **2021**, *122*, 105184. [CrossRef]
29. Xiao, Z.; Shi, X.; Wang, X.; Ma, X.; Han, Y. Lubrication analysis and wear mechanism of heavily loaded herringbone gears with profile modifications in full film and mixed lubrication point contacts. *Wear* **2021**, *477*, 203790. [CrossRef]
30. Cao, P.; Li, Q.; Feng, K.; Qin, Y. Dynamic modeling of spur gear transmission system with evolutive coupling fault of fatigue crack and wear. *Eng. Fail. Anal.* **2024**, *156*, 107820. [CrossRef]
31. Zhang, X.; Zhong, J.; Li, W.; Bocian, M. Nonlinear dynamic analysis of high-speed gear pair with wear fault and tooth contact temperature for a wind turbine gearbox. *Mech. Mach. Theory* **2022**, *173*, 104840. [CrossRef]
32. Yan, Y.; Jiang, C.; Li, W. Simulation on coupling effects between surface wear and fatigue in spur gear. *Eng. Fail. Anal.* **2022**, *134*, 106055. [CrossRef]
33. Huangfu, Y.; Dong, X.; Cao, Y.; Li, Z.; Peng, Z.; Sun, Y. A life-cycle dynamic wear degradation model of planetary gear systems. *Wear* **2024**, *542–543*, 205281. [CrossRef]
34. Feng, K.; Borghesani, P.; Smith, W.A.; Randall, R.B.; Chin, Z.Y.; Ren, J.; Peng, Z. Vibration-based updating of wear prediction for spur gears. *Wear* **2019**, *426–427*, 1410–1415. [CrossRef]
35. Feng, K.; Smith, W.A.; Peng, Z. Use of an improved vibration-based updating methodology for gear wear prediction. *Eng. Fail. Anal.* **2021**, *120*, 105066. [CrossRef]
36. Li, W.; Hao, L.J. Study on the degradation law of harmonic gear drive backlash with wear and assembly errors. *Eng. Fail. Anal.* **2022**, *140*, 106614. [CrossRef]
37. Peng, X.; Zhou, J. Optimization design for dynamic characteristics of face gear drive with surface-active modification. *Mech. Mach. Theory* **2022**, *176*, 105007. [CrossRef]
38. Gottwald, G.A.; Melbourne, I. On the Implementation of the 0–1 Test for Chaos. *SIAM J. Appl. Dyn. Syst.* **2009**, *8*, 129–145. [CrossRef]

Disclaimer/Publisher's Note: The statements, opinions and data contained in all publications are solely those of the individual author(s) and contributor(s) and not of MDPI and/or the editor(s). MDPI and/or the editor(s) disclaim responsibility for any injury to people or property resulting from any ideas, methods, instructions or products referred to in the content.